The First Combined Hα and Rest-UV Spectroscopic Probe of Galactic Outflows at High Redshift

Emily Kehoe,[1] Alice E. Shapley,[1] N.M. Förster Schreiber,[2] Anthony J. Pahl,[3] Michael W. Topping,[4]
Naveen A. Reddy,[5] Reinhard Genzel,[2] Sedona H. Price,[6] and L.J. Tacconi[2]

[1] Department of Physics & Astronomy; University of California, Los Angeles; Los Angeles, CA 90095, USA
[2] Max-Planck-Institut für Extraterrestiche Physik (MPE); Giessenbachstr., 85748, Garching, Germany
[3] The Observatories of the Carnegie Institution for Science; 813 Santa Barbara Street; Pasadena, CA 91101, USA
[4] Department of Astronomy / Steward Observatory; University of Arizona; 933 N Cherry Ave; Tucson, AZ 85721, USA
[5] Department of Physics & Astronomy; University of California, Riverside; 900 University Avenue; Riverside, CA 92521, USA
[6] Department of Physics and Astronomy and PITT PACC; University of Pittsburgh; Pittsburgh, PA 15260, USA

ABSTRACT

We investigate the multi-phase structure of gas flows in galaxies. We study 80 galaxies during the epoch of peak star formation ($1.4 \leq z \leq 2.7$) using data from Keck/LRIS and VLT/KMOS. Our analysis provides a simultaneous probe of outflows using UV emission and absorption features and Hα emission. With this unprecedented data set, we examine the properties of gas flows estimated from LRIS and KMOS in relation to other galaxy properties, such as star formation rate (SFR), star formation rate surface density ($\Sigma_{\rm SFR}$), stellar mass (M_*), and main sequence offset (ΔMS). We find no strong correlations between outflow velocity measured from rest-UV lines centroids and galaxy properties. However, we find that galaxies with detected outflows show higher averages in SFR, $\Sigma_{\rm SFR}$, and ΔMS than those lacking outflow detections, indicating a connection between outflow and galaxy properties. Furthermore, we find a lower average outflow velocity than previously reported, suggesting greater absorption at the systemic redshift of the galaxy. Finally, we detect outflows in 49% of our LRIS sample and 30% in the KMOS sample, and find no significant correlation between outflow detection and inclination. These results may indicate that outflows are not collimated and that Hα outflows have a lower covering fraction than low-ionization interstellar absorption lines. Additionally, these tracers may be sensitive to different physical scales of outflow activity. A larger sample size with a wider dynamic range in galaxy properties is needed to further test this picture.

Keywords: galaxies: evolution – galaxies: high-redshift – galaxies: kinematics and dynamics

1. INTRODUCTION

Galaxy outflows play a crucial role in galaxy evolution over cosmic time, significantly impacting both galaxies and the intergalactic medium (IGM). Galaxy outflows, powered by phenomena such as supernovae, stellar winds, and active galactic nuclei (AGN), serve to regulate the availability of gas for star formation (Heckman 2001; Croton et al. 2006). The relationship between galaxy stellar mass or luminosity and dark matter halo mass is influenced by gas outflows (Madau et al. 1996; Moster et al. 2010; Behroozi et al. 2013). Furthermore, galactic outflows regulate the chemical enrichment histories of galaxies (Davé et al. 2012; Hopkins et al. 2012; Hirschmann et al. 2013; Vogelsberger et al. 2013; Chisholm et al. 2017). Specifically, outflows deplete the amount of cold gas available for star formation and remove metals from galaxies (Scannapieco et al. 2005; Di Matteo et al. 2005; Croton et al. 2006; Somerville et al. 2008; Erb 2015; Beckmann et al. 2017), enriching the circumgalactic medium (CGM) and the IGM (Tremonti et al. 2004; Dalcanton 2007; Finlator & Davé 2008; Peeples et al. 2014; Tumlinson et al. 2017). In other words, the role played by gas outflows in galaxy formation is reflected in the form of the mass-metallicity relation (Davé et al. 2011; Calabrò et al. 2017; Sanders et al. 2018; Fontanot et al. 2021; Sanders et al. 2021) and the fundamental metallicity relation (Mannucci et al. 2010; Sanders et al. 2018, 2021).

The properties of outflows at high redshift have been investigated with both rest-UV interstellar features, such as metal absorption lines and Lyα emission, and broad rest-optical nebular line emission, such as Hα, [N II], [S II], and [O III]. Blueshifted interstellar absorption yields information on the outflowing material that

galaxies have been ejecting throughout time (Shapley et al. 2003; Weiner et al. 2009; Steidel et al. 2010; Kornei et al. 2012; Talia et al. 2012; Bordoloi et al. 2014; Calabrò et al. 2022; Weldon et al. 2022). In rest-frame optical emission line spectra, broad high velocity components trace denser outflowing material that is within a few kiloparsecs of the launching points of outflows (Shapiro et al. 2009; Genzel et al. 2011, 2014; Newman et al. 2012a, 2014; Cano-Díaz et al. 2016; Förster Schreiber et al. 2014; Förster Schreiber et al. 2019; Brusa et al. 2015; Cresci et al. 2015; Harrison et al. 2016; Leung et al. 2017, 2019; Davies et al. 2019, 2020; Freeman et al. 2019; Swinbank et al. 2019; Concas et al. 2022). However, rest-UV absorption and rest-optical nebular emission features tend to provide different answers on the nature of galaxy outflows, such as the detection rate, 3D structure, kinematics, and mass loading factors (Shapley et al. 2003; Steidel et al. 2010; Talia et al. 2012; Förster Schreiber et al. 2019; Davies et al. 2019; Calabrò et al. 2022; Weldon et al. 2022). This discrepancy implies that outflows have a complex and multi-phase structure.

Thus far, no study has investigated rest-optical and rest-UV probes of outflows simultaneously in the same galaxies among the general population at $z \sim 2$, which is vital for understanding the multi-phase structure of outflowing gas. In this study, we analyze a sample of 80 galaxies at $1.4 \leq z \leq 2.7$ using observations obtained from the Low Resolution Imagining Spectrometer (LRIS) (Oke et al. 1995; Steidel et al. 2004) at Keck. At these redshifts, LRIS spectra cover Lyα emission and various low-ionization interstellar (LIS) absorption lines that probe wind kinematics (i.e., Si II λ1260, O I λ1302, Si II λ1304, C II λ1334, and Si II λ1527) as well as the frequency of outflow detections. We draw our sample from the KMOS^{3D} survey (Wisnioski et al. 2015, 2019), which uses the K-Band Multi Object Spectrograph (KMOS) at the Very Large Telescope (VLT) to spatially and spectrally resolve the Hα+[N II]+[S II] line emission of $z \sim 0.7 - 2.7$ star-forming galaxies. As part of the KMOS^{3D} survey, the demographics and properties of galactic-scale outflows were studied by Genzel et al. (2014) and Förster Schreiber et al. (2019).

We use this unique data set to study the correlation between outflow detection and galaxy properties by looking at the frequency of outflows determined from LRIS and KMOS. One of the primary objectives of this paper is to look for any trends between outflow velocities and galaxy properties, such as inclination (i), star formation rate (SFR), SFR surface-density (Σ_{SFR}), stellar mass (M$_*$), and main sequence offset (ΔMS). Furthermore, based on the unique combination of both rest-UV interstellar features and Hα emission probes of outflows,

we aim to analyze the outflow kinematics and investigate the geometry of galactic outflows.

The outline of this paper is as follows: Section 2 introduces our observations, data reduction, and the final sample used for our analysis. Section 3 describes the methods for measuring galactic properties (i.e., outflow velocity, i, SFR, Σ_{SFR}, M$_*$, and ΔMS). Section 4 presents the results of our analysis of the correlations between outflow properties inferred from both LRIS and KMOS observations. Section 5 discusses the implications of our key results. Throughout this paper, we adopt a ΛCDM cosmology with $H_0 = 70$ km s^{-1}, $\Omega_m = 0.3$, $\Omega_{\Lambda} = 0.7$ and the Chabrier (2003) stellar initial mass function (IMF).

2. DATA

2.1. KMOS^{3D} Survey

The KMOS^{3D} survey was conducted with the multi-IFU instrument KMOS at the VLT (Wisnioski et al. 2015, 2019) and focused on galaxies selected from the 3D-HST catalog (Momcheva et al. 2016). The survey observed Hα, [N II], and [S II] emission in the YJ, H, and K bands for galaxies spanning a redshift range of $z = 0.7$–2.7. Building on earlier work on outflows based on near-IR IFU observations with SINFONI from the SINS/zC-SINF survey (Shapiro et al. 2009; Genzel et al. 2011; Newman et al. 2012a,b; Förster Schreiber et al. 2014) and the first-year sample from KMOS^{3D} (Genzel et al. 2014), Förster Schreiber et al. (2019) exploited the completed KMOS^{3D} survey data supplemented with smaller sets from SINS/zC-SINF and slit spectroscopic campaigns (Kriek et al. 2007, 2008; Genzel et al. 2013; Newman et al. 2014; van Dokkum et al. 2015) to characterize outflow demographics and properties.

The full sample of 599 galaxies (525 from KMOS^{3D}) was used to search for a broad outflow emission signature in Hα+[N II]+[S II] emission, evident as residual high-velocity wings underneath the star formation-dominated narrow component in "velocity-shifted" spectra. The IFU data allow mapping of the velocity field derived from the emission line peak, which can then be used to align the spectra of individual spaxels across the galaxies to a common peak velocity. The aligned spectra are then added together to create "velocity-shifted" spectra. This technique removes the line broadening caused by gravitational motions (e.g., disk rotation), facilitating the identification of high-velocity components from outflows. For cases with identified outflow signature, Förster Schreiber et al. (2019) attributed the outflow driver to star formation or AGN primarily on the basis of whether an AGN was identified through independent indicators (see below for more detail) as well as on the

basis of the narrow [N II]/Hα ratio. In total, Förster Schreiber et al. (2019) found that within the KMOS³ᴰ survey there are 190 out of 599 galaxies at $1.4 \leq z \leq 2.7$ with a broad-component outflow signature, yielding an outflow detection fraction of 32%. Among galaxies with outflow signatures, there are 87 galaxies with SF-driven winds (46%) and 103 galaxies with AGN-driven winds (54%).

2.2. KMOS-LRIS Observations

2.2.1. Sample Selection

In constructing a sample for follow-up LRIS observations, we selected 85 galaxies from the KMOS³ᴰ survey (Wisnioski et al. 2015). These targets lie in the COSMOS and GOODS-S extragalactic legacy fields, and are covered by extensive existing multi-wavelength datasets. The mask design included all galaxies with KMOS emission line detections, prioritizing galaxies at $z > 1.5$ with higher data quality (i.e., higher S/N and adaptive optics) and the presence of outflow signatures in KMOS detected by Förster Schreiber et al. (2019). Out of the 85 galaxies targeted with LRIS, 33 (39%) were identified as having outflows from the KMOS³ᴰ survey. Specifically, 19 (22%) of the targets have SF-driven outflows, 14 (16%) of the targets have AGN-driven outflows, and 52 (61%) of the targets had no outflow detection. As shown in Figure 1, our final sample spans a redshift range of $1.50 \leq z \leq 2.68$.

2.2.2. Observations

We observed 85 KMOS³ᴰ galaxies using the Keck Low-Resolution Imaging Spectrometer (LRIS) (Oke et al. 1995; Steidel et al. 2004) over six and a half nights, including 4 nights in December of 2019 and 2.5 nights in January of 2021. Our observations use four multi-object slit masks: two in the COSMOS and two in the GOODS-S fields. All masks used 1.2" slits. We employed the d500 dichroic for the December 2019 run with the 400 lines mm^{-1} grism blazed at 3400 Å on the blue side and the 600 lines mm^{-1} grating blazed at 5000 Å on the red side. In January 2021, due to red-side instrument problems, we only collected data on the blue side. For these observations, we used the d680 dichroic and the 400 lines mm^{-1} grism. In our analysis we only use the blue side data, as it covers the rest-UV features of interest for all of our target galaxies. LRIS blue-side spectra yielded a resolution of R ∼ 800. With this configuration, we have continuous wavelength coverage from the 3100 Å atmospheric cut-off up to the d500 dichroic cut-off at 5000 Å for 43 spectra taken during the December 2019 run. The remaining spectra taken with the d680 dichroic have varying red wavelength cut-offs that range

from 5200-7650 Å depending on the horizontal location of the slit on the multi-slit mask. Exposure times ranged from 5 to 19 hours. Weather conditions during the December 2019 run were poor, permitting data collection during only 1.5 of the 4 scheduled nights. When it was at least partially clear, seeing ranged from 0.5 to 1.3 arcsec. Conditions were clear throughout the 2.5 nights of the January 2021 run, with seeing ranging from 0.65 to 1.1 arcsec. A summary of the masks used during our LRIS observations is provided in Table 1.

2.2.3. Data Reduction

Blue-side LRIS data reduction was performed using custom IRAF, IDL, and Python scripts. The first step was to rectify each spectrum by fitting a polynomial to each 2D slit and transforming them to be rectangular. Next, we flat-fielded each exposure and cut out the slits for each object. Additionally, we background subtracted each object by removing cosmic rays and creating bad-pixel maps. We then created a summed mosaic of the 2D spectra, including science, arc and sky images, by first calculating the offsets between the individual science exposures, shifting, and averaging them. We performed a secondary background subtraction to avoid overestimating the background. After the initial background subtraction, many of the spectra sit in troughs with negative fluxes on each side of the spectrum. This trough arises from fitting a polynomial to the light across the entire slit. The light from the object biases the fit, overestimating the background. The second pass background subtraction excludes the object from the fit, removing any bias. To further ensure the accuracy of the background subtraction, we identified the locations of bright emission lines within the 2D spectra to mask any object traces and broaden the region around the emission lines, since the object trace is wider in these regions. Applying the newly defined masks prevents oversubtraction in these specific regions. Using these second pass images, we fit a line or a polynomial of order 2 to the science trace of each exposure to extract 1D spectra from our stacked 2D spectra. We applied the same extraction aperture to the arc and sky spectra. We then used the arc spectrum to determine the wavelength solution, which we applied to the sky spectrum. Following this step, we used the wavelengths of the bright sky lines to determine any required zero point shift in the wavelength solution. Finally, we flux calibrated our data using standard star observations.

Most of our masks were collected during one epoch. However, the co_kl1 mask data was collected during both

Table 1. Summary of LRIS observations

Field	Mask Name	RA	Dec.	t_{Blue}^{exp} (s)	$N_{targets}$[a]	$N_{success}$[b]
COSMOS	co_kl1	10:00:24.620	+02:15:13.078	76 540	23	19
COSMOS	co_kl2	10:00:29.041	+02:24:24.528	41 400	20	13
GOODS-S	gs_kl1	03:32:30.639	-27:48:24.384	46 200	20	9
GOODS-S	gs-kl2	03:32:28.728	-27:43:29.212	17 400	22	17

[a] Total number of targets on each mask.

[b] Total number of successful extractions.
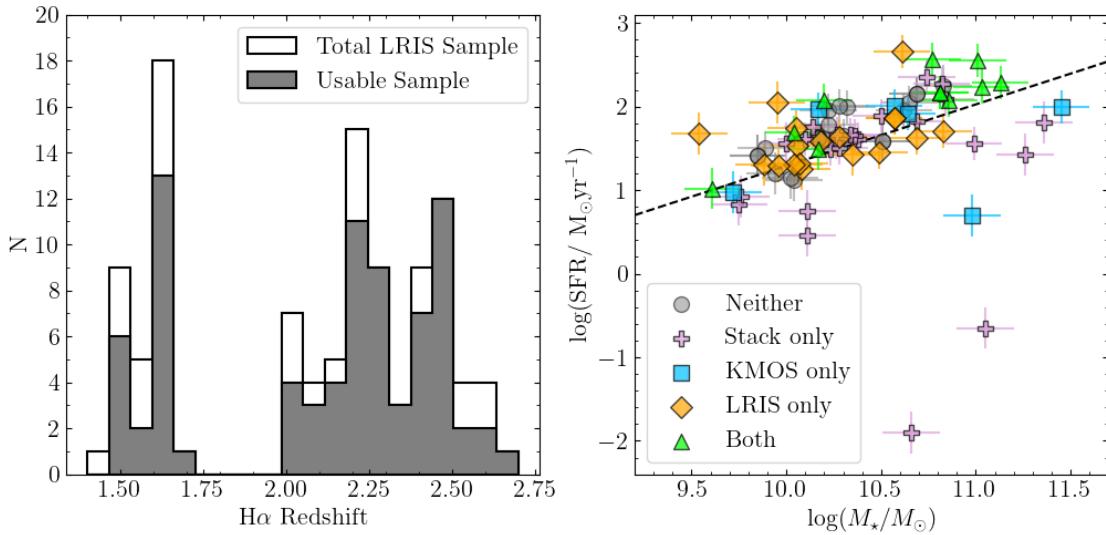
Figure 1. Properties of the full LRIS sample. *Left:* Hα redshift distributions for the LRIS sample. The open histogram represents the total sample (107 objects), and the gray histogram represents the sample of objects that had a usable spectrum for our analysis (80 objects). *Right:* SFR versus stellar mass. SFRs and stellar masses are derived from Förster Schreiber et al. (2019) who followed procedures by Wuyts et al. (2011). Gray circles are galaxies where outflows were not detected in either KMOS or LRIS (23 objects), purple crosses represent galaxies that were only used in creating stacked spectra because no significant line measurements were found (23 objects), blue squares are galaxies where outflows were detected in KMOS (6 objects), orange diamonds are galaxies where outflows were detected with only LRIS (17 objects), and green triangles are galaxies that where outflows were detected with both KMOS and LRIS (11 objects). LRIS outflows are identified in galaxies with Δv_{LIS}, $\Delta v_{Ly\alpha}$, or both significantly offset from the systemic velocity. The dashed line represents the SFR main sequence for $z \sim 2$ from Speagle et al. (2014).

the December 2019 and January 2021 runs. The reductions for each run were done separately up to the 1D extractions. We combined the 1D spectra of each galaxy using a S/N-weighted average. As listed in Table 1, we successfully extracted 58 usable spectra ($N_{success}$) out of our 85 targets ($N_{targets}$). The remaining 27 spectra were either too noisy or had artifacts, making them unusable for our analysis.

2.2.4. *MOSDEF-LRIS Observations*

We expanded our sample of KMOS[3D] galaxies with LRIS observations by incorporating observations from the MOSDEF-LRIS survey, described in detail by Topping et al. (2020), Reddy et al. (2022), and Weldon et al. (2022). These MOSDEF-LRIS galaxies have KMOS[3D] coverage and fall within the same redshift range as the rest of the KMOS-LRIS sample (i.e., they satisfy the same selection criteria as the galaxies for which we obtained new LRIS observations). This LRIS survey targeted galaxies with existing MOSFIRE observations from the MOSFIRE Deep Evolution Field (MOSDEF)

survey (Kriek et al. 2015) and includes LRIS spectra with similar depth and the same observational setup as data we collected. The MOSDEF-LRIS and KMOS^{3D} surveys both target the COSMOS and GOODS-S fields and have 22 galaxies in common. We integrate these observations into this paper to expand our KMOS^{3D} sample with usable LRIS spectra from 58 to 80 galaxies.

3. MEASUREMENTS

3.1. Outflow Velocities

Large-scale gas outflows cause Doppler shifts in low-ionization interstellar (LIS) absorption lines and Lyα emission relative to the galaxy's systemic velocity. To quantify these shifts, we measure the line centroid velocity shifts, $\Delta v_{\rm LIS}$ and $\Delta v_{\rm Ly\alpha}$, from the centroid wavelengths, respectively, of strong LIS absorption lines and Lyα emission. We first determined which lines were significantly-detected by using a non-parametric estimate of the line flux, which was used to find the equivalent width (EW) of each line. When determining the EW, we defined the continuum using blue and red wavelength windows around each line. These windows were defined using a stacked spectrum of the entire sample, ensuring a high S/N to provide a precise average for where the continuum lies. The wavelength windows are listed in Table 2. Uncertainties on the flux measurements were determined using Monte Carlo simulations in which each spectrum was perturbed on a pixel-by-pixel basis according to the error spectrum over 1000 iterations. If the absolute values of line fluxes were greater than 2σ, we labeled the line as being significantly-detected. For each significantly-detected line, we measured the observed centroids for the LIS absorption lines and the Lyα emission line, $\lambda_{\rm LIS,\ obs}$ and $\lambda_{\rm Ly\alpha,\ obs}$, respectively, by fitting Gaussian curves to the lines. Uncertainties for the centroid measurements were found using the same Monte Carlo simulations. We shifted $\lambda_{\rm LIS,\ obs}$ and $\lambda_{\rm Ly\alpha,\ obs}$ to the rest frame defined by the object's Hα redshift measured in the KMOS^{3D} survey by Förster Schreiber et al. (2019) (i.e., $\lambda_{\rm LIS} = \lambda_{\rm LIS,\ obs}/(1+z_{\rm H\alpha})$ and $\lambda_{\rm Ly\alpha} = \lambda_{\rm Ly\alpha,\ obs}/(1+z_{\rm H\alpha})$). We use these centroids to measure the line centroid velocity shifts:

$$\Delta v_{\rm LIS} = \frac{\lambda_{\rm LIS} - \lambda_{\rm LIS,\ rest}}{\lambda_{\rm LIS,\ rest}} \times c \qquad (1)$$

$$\Delta v_{\rm Ly\alpha} = \frac{\lambda_{\rm Ly\alpha} - \lambda_{\rm Ly\alpha,\ rest}}{\lambda_{\rm Ly\alpha,\ rest}} \times c \qquad (2)$$

where $\lambda_{\rm LIS,\ rest}$ and $\lambda_{\rm Ly\alpha,\ rest}$ are the laboratory wavelengths for these features as listed in Table 2. From our total sample of 80 usable galaxies, 57 (67%) were found

to have at least one significant rest-UV line measurement in the LRIS spectra. To find $\Delta v_{\rm LIS}$, we calculated an inverse-variance-weighted average of the individual $\Delta v_{\rm LIS}$ measurements for every object that had at least one significantly-detected LIS line. The LIS lines used in the weighted average were Si IIλ1260, C IIλ1334, and Si IIλ1526. We do not include the blend of O IIλ1302+ Si IIλ1304 in our measurements because the blend centroid wavelength is harder to constrain. Velocities that were greater in magnitude than 1σ from zero were defined as having a significant flow. Based on the error bars presented in Table 3, the minimum outflow velocity we can detect is $15 - 20$ km/s in the highest S/N cases.

Out of the 57 significant LIS line measurements, 19 were found to have a significantly-detected outflow (i.e., negative velocity) and 6 were found to have a significantly-detected inflow (i.e., positive velocity). In terms of Lyα kinematics, 17 objects had a significantly-detected outflow (i.e., positive velocity) and 2 objects had a significantly-detected inflow (i.e., negative velocity). Specifically, 11 galaxies show a significant outflow detected solely from LIS absorption lines, 9 galaxies have significant outflows detected exclusively from Lyα emission, and 9 galaxies have significant outflows detected in both. Outflows may only be detected from only Lyα emission because galaxies may have weak absorption lines, but strong Lyα emission. Conversely, galaxies detected by only LIS absorption may show only strong broad Lyα absorption (Shapley et al. 2003). Indeed, the Lyα profile is complex and can range from well-detected emission to strong, broad absorption. In the case of such strong absorption, no meaningful $\Delta v_{\rm Ly\alpha}$ can be measured. Figure 2 shows the distribution of our velocity offset measurements. The mean $\Delta v_{\rm LIS}$ for our sample is -56 ± 16 km s^{-1} and the mean $\Delta v_{\rm Ly\alpha}$ is $+266 \pm 41$ km s^{-1}. The magnitudes of the $\Delta v_{\rm LIS}$ and $\Delta v_{\rm Ly\alpha}$ are not strongly correlated.

We do not present outflow velocities from Hα measurements because the FWHM as a measure of outflow velocity differs from the centroid shifts used for LIS and Lyα in LRIS measurements. The velocity offsets based on centroids of broad components from KMOS^{3D} stacked spectra are generally modest and poorly constrained, except for stronger outflows. Accordingly, comparing kinematic measurements from the two samples is nontrivial. Additionally, emission and absorption lines trace material differently, with Hα more sensitive to denser gas due to its electron density dependence (Förster Schreiber et al. 2019), typically tracing material closer to the galaxy compared to the more extended regions traced by LIS.

Table 2. Spectral windows for line fitting

Line[a]	$\lambda_{\rm rest}$ (Å)	Blue Window (Å)[b]	Red Window (Å)[b]
Lyα	1215.67	$1195 - 1205$	$1229 - 1234$
Si II	1260.42	$1249 - 1235$	$1280 - 1286$
O I + Si II	1303.27	$1286 - 1291$	$1317 - 1323$
C II	1334.53	$1323 - 1329$	$1348 - 1354$
Si II	1526.71	$1511 - 1517$	$1560 - 1566$

[a] O I $\lambda 1302$ + Si II $\lambda 1304$ are blended at the resolution of our LRIS spectra.

[b] The blue and red windows are the wavelength intervals over which local continuum fitting was performed for each feature.

As shown in Table 3, 57 galaxies had at least one feature measured with the LRIS spectra. Out of this sample, 17 galaxies had a significant outflow detected with LRIS only, 6 galaxies had a significant outflow detected with KMOS only, 11 had significant detections with both LRIS and KMOS, and 23 had a detection from neither LRIS or KMOS. The detection fraction of outflows with LRIS and KMOS was 49% (28 out of 57 galaxies) and 30% (17 out of 57 galaxies), respectively.

Furthermore, we measure the maximum outflow velocity ($v_{\rm max}$) by using methods described by Kornei et al. (2012) and Weldon et al. (2022). In summary, we determine the minimum of each LIS absorption line and evaluate the sum of the flux and its uncertainty at each wavelength increment. The spectrum is evaluated at shorter wavelengths until the sum of flux plus uncertainty surpasses 1.0. The first wavelength at which this occurs is the wavelength used to calculate the $v_{\rm max}$. Uncertainties are found using the same Monte Carlo simulations previously described.

3.2. *Galaxy Properties*

We derive several galaxy properties such as SFR, $\Sigma_{\rm SFR}$, M_*, ΔMS, and inclination (Table 4) to investigate how outflow velocity depends on these properties.

SFR, $\Sigma_{\rm SFR}$, M_*, and ΔMS were presented previously in Förster Schreiber et al. (2019). SFR and M_* were determined by modeling the broad- and medium-band spectral energy distributions (SEDs) spanning the optical to near-infrared range for each galaxy and supplemented with *Spitzer* and *Herschel* mid and far-IR photometry when available. SEDs were fit using Bruzual & Charlot (2003) population synthesis models
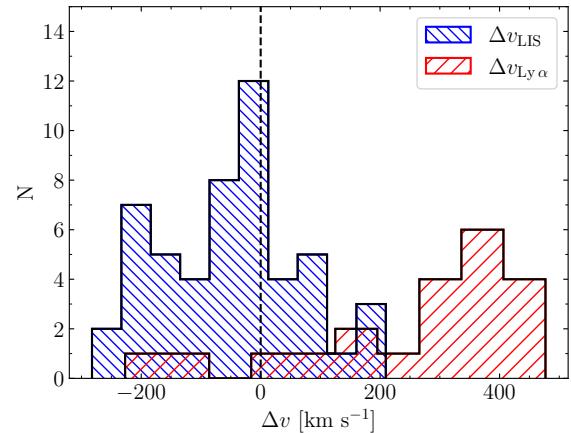

Figure 2. Velocity offset distribution. The blue hashed histogram represents centroid velocity shifts for LIS absorption lines and the red hashed histogram represents centroid velocity shifts for Lyα emission. In total, there are 57 objects with at least one feature. 51 objects had LIS velocity measurements with $\langle \Delta v_{\rm LIS} \rangle = -56 \pm 16 {\rm km~s}^{-1}$ and 21 objects had Lyα velocity measurements with $\langle \Delta v_{\rm Ly\alpha} \rangle = 266 \pm 41 {\rm km~s}^{-1}$.

that adopted the Calzetti et al. (2000) reddening law, solar metallicty, and SF histories. Furthermore, Förster Schreiber et al. (2019) adopt a Chabrier (2003) stellar initial mass function. There were 34 galaxies for which the SFR was determined by fitting SEDs across optical to *Spitzer*/IRAC wavelengths. The remaining 73 galaxies had their SFR determined by combining the SFRs from *Herschel/Spitzer* + UV. SFR and M_* uncertainties were adopted from Tacconi et al. (2018). An uncertainty of ± 0.25 dex is used for SED-inferred SFRs, while an uncertainty ± 0.2 dex is used for *Herschel/Spitzer*-detected galaxies. We define the $\Sigma_{\rm SFR}$ as:

$$\Sigma_{\rm SFR} = \frac{\rm SFR}{2\pi R_e^2} \qquad (3)$$

Table 3. Measurements and detections for galactic outflows

Object	RA	Dec	$z_{\mathrm{H}\alpha}$	Δv_{LIS}[a]	Δv_{Lya}[a]	Δv_{max}[a]	LRIS Outflow[b]	KMOS Outflows[c]	AGN[d]
				[km s^{-1}]	[km s^{-1}]	[km s^{-1}]			
COS4_12476	10:00:27.638	+02:18:24.773	1.5143	-130 ± 43	...	-187 ± 109	1	0	0
COS4_24738	10:00:33.201	+02:26:02.811	1.5888	19 ± 94	...	-287 ± 208	0	0	0
COS4_12056	10:00:31.208	+02:18:09.725	1.6000	113 ± 282	...	-225 ± 197	0	1	0
GS4_39085	03:32:17.113	−27:43:42.067	1.6100	...	402 ± 526	...	1	0	0
GS4_08422	03:32:37.761	−27:52:12.306	1.6113	-33 ± 42	...	-87 ± 282	0	1	1
GS4_44066	03:32:25.165	−27:42:18.785	1.6140	...	476 ± 259	...	1	1	1
GS4_11203	03:32:36.206	−27:51:29.923	1.6144	-98 ± 80	...	-285 ± 153	1	0	0
COS4_11343	10:00:35.251	+02:17:43.035	1.6474	13 ± 29	-98 ± 54	-346 ± 86	0	0	1
COS4_18358	10:00:40.111	+02:22:00.462	1.6484	-20 ± 49	399 ± 19	-75 ± 107	1	1	0
COS4_20595	10:00:39.360	+02:23:20.651	1.6547	-183 ± 19	444 ± 26	-118 ± 74	1	0	0
COS4_20449	10:00:28.246	+02:23:15.611	1.6559	-46 ± 50	...	-300 ± 87	0	0	0
COS4_17519	10:00:36.870	+02:21:30.183	1.7081	105 ± 152	...	-220 ± 158	0	0	0
COS4_18604	10:00:31.758	+02:22:08.159	2.0055	-162 ± 89	...	-518 ± 99	1	0	0
COS4_20746	10:00:38.767	+02:23:27.429	2.0070	-282 ± 84	...	-445 ± 73	1	0	0
GS4_20410	03:32:21.950	−27:48:55.602	2.0085	19 ± 100	...	-158 ± 165	0	0	0
COS4_13174	10:00:26.935	+02:18:50.313	2.0974	-278 ± 184	270 ± 25	-396 ± 224	1	1	0
GS4_42363	03:32:28.410	−27:42:46.562	2.1408	-218 ± 26	...	-563 ± 51	1	1	0
GS4_41886	03:32:23.436	−27:42:55.015	2.1411	...	271 ± 9	...	1	1	1
COS4_08775	10:00:16.549	+02:16:09.402	2.1624	-122 ± 84	372 ± 34	-287 ± 162	1	0	0
COS4_13701	10:00:27.052	+02:19:09.982	2.1664	-41 ± 51	...	-113 ± 137	0	1	0
COS4_25229	10:00:26.019	+02:26:22.974	2.1807	-72 ± 17	...	-430 ± 41	1	0	0
GS4_38116	03:32:41.113	−27:43:58.606	2.1966	-26 ± 131	...	...	0	0	0
GS4_38116	03:32:41.113	−27:43:58.606	2.1966	-30 ± 116	...	...	0	0	0
COS4_09044	10:00:35.706	+02:16:19.384	2.1983	-16 ± 44	...	-191 ± 131	0	0	0
GS4_25151	03:32:23.914	−27:47:39.386	2.2229	175 ± 81	...	-240 ± 122	0	0	0
GS4_29868	03:32:29.066	−27:46:28.614	2.2239	-29 ± 56	...	-371 ± 107	0	0	0
COS4_04930	10:00:29.037	+02:13:43.661	2.2273	66 ± 77	...	-731 ± 132	0	0	0
COS4_04930	10:00:29.037	+02:13:43.661	2.2273	66 ± 79	...	-69 ± 194	0	0	0
COS4_04519	10:00:28.641	+02:13:26.952	2.2285	-185 ± 80	223 ± 98	-948 ± 96	1	0	0
COS4_06963	10:00:18.380	+02:14:58.858	2.3012	-213 ± 216	-227 ± 59	-148 ± 451	0	1	0
GS4_41748	03:32:24.196	−27:42:57.553	2.3013	...	109 ± 54	...	1	0	1
COS4_05389	10:00:17.593	+02:13:58.786	2.3013	-42 ± 97	...	-399 ± 167	0	1	0
GS4_40768	03:32:09.797	−27:43:08.645	2.3033	82 ± 19	...	-290 ± 43	0	0	1
GS4_36705	03:32:10.189	−27:44:16.303	2.3055	-54 ± 26	378 ± 18	-152 ± 118	1	0	0
COS4_01966	10:00:30.209	+02:11:57.563	2.3058	-1 ± 201	...	-295 ± 261	0	0	0
COS4_03324	10:00:35.618	+02:12:47.281	2.3069	-65 ± 118	...	-112 ± 219	0	0	0
COS4_02672	10:00:31.073	+02:12:25.912	2.3077	-212 ± 50	...	-634 ± 96	1	0	0
COS4_02672	10:00:31.073	+02:12:25.912	2.3077	-80 ± 73	328 ± 66	-521 ± 241	1	0	0
GS4_38807	03:32:43.633	−27:43:47.712	2.3177	-215 ± 263	...	-258 ± 261	0	0	0
GS4_35937	03:32:38.139	−27:44:33.630	2.3292	-224 ± 124	...	-137 ± 238	1	0	1
GS4_46938	03:32:32.294	−27:41:26.362	2.3323	-80 ± 15	294 ± 8	-40 ± 73	1	1	0
GS4_45188	03:32:15.182	−27:41:58.693	2.4061	-186 ± 103	146 ± 40	-225 ± 379	1	1	1
GS4_45188	03:32:15.182	−27:41:58.693	2.4061	-35 ± 274	374 ± 103	-924 ± 168	1	1	1
GS4_40679	03:32:19.057	−27:43:15.143	2.4079	209 ± 67	...	-508 ± 374	0	0	0
GS4_40679	03:32:19.057	−27:43:15.143	2.4079	209 ± 63	...	-157 ± 115	0	0	0
GS4_38560	03:32:18.726	−27:43:51.672	2.4165	-146 ± 134	...	-396 ± 216	1	0	0
COS4_06079	10:00:26.272	+02:14:24.258	2.4413	...	25 ± 55	...	0	1	0
COS4_17298	10:00:32.355	+02:21:21.002	2.4443	-98 ± 29	430 ± 15	-442 ± 55	1	0	0
GS4_40218	03:32:38.869	−27:43:21.565	2.4504	62 ± 28	...	-235 ± 224	0	0	0
GS4_40218	03:32:38.869	−27:43:21.565	2.4504	27 ± 25	...	-271 ± 67	0	0	0
GS4_45068	03:32:33.016	−27:42:00.378	2.4527	...	161 ± 18	...	1	1	1
COS4_08515	10:00:44.275	+02:15:58.544	2.4539	9 ± 105	429 ± 12	-31 ± 156	1	0	0
COS4_12148	10:00:28.499	+02:18:09.696	2.4603	4 ± 61	...	-262 ± 128	0	0	0
COS4_22995	10:00:17.153	+02:24:52.319	2.4681	-34 ± 165	364 ± 43	-657 ± 207	1	1	1
COS4_22564	10:00:17.563	+02:24:42.596	2.4694	-26 ± 81	...	-562 ± 75	0	0	0
COS4_27120	10:00:24.075	+02:27:45.211	2.4780	-171 ± 60	...	-336 ± 112	1	1	0
COS4_27087	10:00:24.214	+02:27:41.260	2.4794	-149 ± 37	...	-677 ± 67	1	0	0

[a] "..." indicates that no significant ($> 2\sigma$) detections of LIS or Lyα features were made in the LRIS spectrum.

[b] A significant LRIS outflow detection is denoted with 1, while a non-significant detection is denoted with 0. A detection is classified as significant when the measured Δv_{LIS} or $\Delta v_{\mathrm{Ly}\alpha}$ is greater in magnitude than 1σ from 0.

[c] A KMOS outflow detection is denoted with 1, while a non-detection is denoted with 0. Detections are found from SF or AGN broad emission line signatures.

[d] Galaxies hosting AGN based on Hα multi-wavelength analysis or rest-UV spectra are denoted with 1 and galaxies without AGN are denoted as 0. 10 out of the 15 AGNs in our sample have individual gas kinematic measurements.

Table 4. Galactic properties for the full KMOS-LRIS sample

Object	$z_{H\alpha}$	i (degrees)	$\log(SFR/(M_\odot yr^{-1}))$	$\log(\Sigma_{SFR}/(M_\odot yr^{-1} kpc^{-2}))$	$\log(M_*/M_\odot)$	ΔMS
COS4_12476	1.5143	59 ± 0.02	1.75 ± 0.2	0.4 ± 0.13	10.05 ± 0.15	0.5 ± 0.2
COS4_24738	1.5888	49 ± 0.04	1.15 ± 0.25	-0.49 ± 0.03	10.02 ± 0.15	-0.1 ± 0.25
COS4_12056	1.6000	55 ± 0.03	0.98 ± 0.25	-1.31 ± 0.0	9.72 ± 0.15	0.01 ± 0.25
GS4_39085	1.6100	44 ± 0.03	1.45 ± 0.2	-0.17 ± 0.06	10.49 ± 0.15	-0.15 ± 0.2
GS4_08422	1.6113	31 ± 0.03	2.0 ± 0.2	1.62 ± 1.34	11.45 ± 0.15	-0.18 ± 0.2
GS4_44066	1.6140	27 ± 0.03	2.56 ± 0.2	1.97 ± 4.69	10.77 ± 0.15	0.78 ± 0.2
GS4_11203	1.6144	45 ± 0.04	1.29 ± 0.2	0.49 ± 0.19	9.96 ± 0.15	0.09 ± 0.2
COS4_11343	1.6474	53 ± 0.02	1.51 ± 0.2	-0.49 ± 0.02	9.89 ± 0.15	0.37 ± 0.2
COS4_18358	1.6484	53 ± 0.03	1.02 ± 0.25	-0.46 ± 0.02	9.61 ± 0.15	0.15 ± 0.25
COS4_20595	1.6547	58 ± 0.01	1.25 ± 0.25	-0.34 ± 0.02	10.08 ± 0.15	-0.08 ± 0.25
COS4_20449	1.6559	34 ± 0.03	1.12 ± 0.25	-0.74 ± 0.01	10.04 ± 0.15	-0.17 ± 0.25
COS4_17519	1.7081	39 ± 0.02	2.0 ± 0.2	0.16 ± 0.05	10.32 ± 0.15	0.49 ± 0.2
COS4_18604	2.0055	64 ± 0.02	1.53 ± 0.2	-0.17 ± 0.03	10.06 ± 0.15	0.11 ± 0.2
COS4_20746	2.0070	32 ± 0.06	1.32 ± 0.25	0.23 ± 0.08	10.07 ± 0.15	-0.11 ± 0.25
GS4_20410	2.0085	56 ± 0.01	1.63 ± 0.2	-0.04 ± 0.02	10.2 ± 0.15	0.08 ± 0.2
COS4_13174	2.0974	73 ± 0.02	2.24 ± 0.2	-0.15 ± 0.05	11.03 ± 0.15	0.1 ± 0.2
GS4_42363	2.1408	68 ± 0.01	2.07 ± 0.2	0.65 ± 0.13	10.2 ± 0.15	0.48 ± 0.2
GS4_41886	2.1411	54 ± 0.02	2.07 ± 0.2	0.99 ± 0.42	10.86 ± 0.15	0.04 ± 0.2
COS4_08775	2.1624	55 ± 0.02	1.43 ± 0.25	-0.47 ± 0.02	10.35 ± 0.15	-0.26 ± 0.25
COS4_13701	2.1664	50 ± 0.02	1.92 ± 0.2	-0.08 ± 0.04	10.64 ± 0.15	0.03 ± 0.2
COS4_25229	2.1807	48 ± 0.04	1.3 ± 0.25	0.33 ± 0.11	10.04 ± 0.15	-0.14 ± 0.25
GS4_38116	2.1966	64 ± 0.02	1.63 ± 0.2	0.43 ± 0.1	10.17 ± 0.15	0.06 ± 0.2
GS4_38116	2.1966	64 ± 0.02	1.63 ± 0.2	0.43 ± 0.1	10.17 ± 0.15	0.06 ± 0.2
COS4_09044	2.1983	57 ± 0.03	1.2 ± 0.25	0.03 ± 0.06	9.94 ± 0.15	-0.15 ± 0.25
GS4_25151	2.2229	28 ± 0.03	2.05 ± 0.2	-0.2 ± 0.02	10.65 ± 0.15	0.13 ± 0.2
GS4_29868	2.2239	58 ± 0.02	2.01 ± 0.2	-0.18 ± 0.1	10.28 ± 0.15	0.35 ± 0.2
COS4_04930	2.2273	59 ± 0.03	1.59 ± 0.25	-0.36 ± 0.08	10.51 ± 0.15	-0.23 ± 0.25
COS4_04930	2.2273	59 ± 0.03	1.59 ± 0.25	-0.36 ± 0.08	10.51 ± 0.15	-0.23 ± 0.25
COS4_04519	2.2285	50 ± 0.02	2.66 ± 0.2	1.11 ± 0.76	10.61 ± 0.15	0.77 ± 0.2
COS4_06963	2.3012	28 ± 0.07	0.7 ± 0.25	-0.74 ± 0.04	10.98 ± 0.15	-1.46 ± 0.25
COS4_05389	2.3013	47 ± 0.05	1.97 ± 0.2	0.52 ± 0.31	10.17 ± 0.15	0.38 ± 0.2
GS4_41748	2.3013	36 ± 0.03	1.7 ± 0.2	0.61 ± 0.23	10.83 ± 0.15	-0.35 ± 0.2
GS4_40768	2.3033	72 ± 0.01	1.78 ± 0.2	-0.07 ± 0.01	10.22 ± 0.15	0.14 ± 0.2
GS4_36705	2.3055	53 ± 0.02	1.64 ± 0.2	0.41 ± 0.16	10.28 ± 0.15	-0.04 ± 0.2
COS4_01966	2.3058	65 ± 0.06	1.67 ± 0.2	0.01 ± 0.17	10.16 ± 0.15	0.08 ± 0.2
COS4_03324	2.3069	46 ± 0.02	1.96 ± 0.2	-0.18 ± 0.03	10.62 ± 0.15	0.05 ± 0.2
COS4_02672	2.3077	60 ± 0.02	1.86 ± 0.2	-0.17 ± 0.03	10.57 ± 0.15	-0.02 ± 0.2
COS4_02672	2.3077	60 ± 0.02	1.86 ± 0.2	-0.17 ± 0.04	10.57 ± 0.15	-0.02 ± 0.2
GS4_38807	2.3177	64 ± 0.01	1.65 ± 0.2	0.05 ± 0.04	10.3 ± 0.15	-0.04 ± 0.2
GS4_35937	2.3292	68 ± 0.01	1.62 ± 0.2	-0.61 ± 0.02	10.69 ± 0.15	-0.34 ± 0.2
GS4_46938	2.3323	58 ± 0.02	1.69 ± 0.2	0.74 ± 0.19	10.04 ± 0.15	0.22 ± 0.2
GS4_45188	2.4061	25 ± 0.07	2.17 ± 0.2	1.23 ± 1.43	10.81 ± 0.15	0.1 ± 0.2
GS4_45188	2.4061	25 ± 0.07	2.17 ± 0.2	1.23 ± 1.43	10.81 ± 0.15	0.1 ± 0.2
GS4_40679	2.4079	36 ± 0.04	2.15 ± 0.2	0.14 ± 0.2	10.69 ± 0.15	0.17 ± 0.2
GS4_40679	2.4079	36 ± 0.04	2.15 ± 0.2	0.14 ± 0.19	10.69 ± 0.15	0.17 ± 0.2
GS4_38560	2.4165	49 ± 0.02	1.58 ± 0.2	-0.32 ± 0.02	10.18 ± 0.15	-0.05 ± 0.2
COS4_06079	2.4413	46 ± 0.03	2.01 ± 0.2	-0.23 ± 0.03	10.57 ± 0.15	0.11 ± 0.2
COS4_17298	2.4443	30 ± 0.07	1.68 ± 0.25	0.37 ± 0.13	9.54 ± 0.15	0.67 ± 0.25
GS4_40218	2.4504	48 ± 0.03	1.41 ± 0.25	0.23 ± 0.07	9.85 ± 0.15	0.09 ± 0.25
GS4_40218	2.4504	48 ± 0.03	1.41 ± 0.25	0.23 ± 0.07	9.85 ± 0.15	0.09 ± 0.25
GS4_45068	2.4527	14 ± 0.1	2.55 ± 0.2	1.66 ± 3.3	11.01 ± 0.15	0.35 ± 0.2
COS4_08515	2.4539	77 ± 0.02	1.3 ± 0.25	-0.8 ± 0.01	9.88 ± 0.15	-0.05 ± 0.25
COS4_12148	2.4603	49 ± 0.05	1.96 ± 0.2	1.28 ± 1.32	10.22 ± 0.15	0.29 ± 0.2
COS4_22995	2.4681	48 ± 0.03	2.29 ± 0.2	1.33 ± 1.08	11.13 ± 0.15	0.0 ± 0.2
COS4_22564	2.4694	47 ± 0.02	2.25 ± 0.25	0.24 ± 0.1	10.83 ± 0.15	0.16 ± 0.25
COS4_27120	2.4780	56 ± 0.04	1.49 ± 0.25	-0.21 ± 0.08	10.17 ± 0.15	-0.14 ± 0.25
COS4_27087	2.4794	45 ± 0.04	2.05 ± 0.25	0.42 ± 0.14	9.95 ± 0.15	0.63 ± 0.25

The half-light effective radii (R_e) were obtained from van der Wel et al. (2012) and Lang et al. (2014), who base their measurements on the H-band radii corrected to rest-frame 5000Å using average color gradients. Uncertainties in R_e were determined from GALFIT. We define the MS offset (ΔMS) as:

$$\Delta\text{MS} = \log(\text{SFR}/\text{SFR}_\text{MS}) \qquad (4)$$

where SFR_MS is the main sequence SFR for a given M_* and redshift, as parameterized by Whitaker et al. (2014). Uncertainties on ΔMS are adopted to be the same as the uncertainties for the SFR.

Galaxy inclination (i) was calculated using the galaxy's axis ratio (q), where q is the ratio of the minor to major axes. Neglecting the intrinsic thickness of the disk, we estimated $i = \arccos(q)$. [1] Axis ratios were obtained from van der Wel et al. (2012) based on the 3D-HST catalogs.

3.3. AGN Identification

From the sample of 80 galaxies used in our analysis, 12 are identified as hosting an AGN (15%) on the basis of the narrow component [N II]/Hα flux ratio and diagnostics from supplementary X-ray to mid-IR and radio data. Galaxies are identified as having an AGN when [N II]/Hα$_\text{narrow} > 0.45$, or when characteristics indicative of an AGN are found in the radio, mid-IR, or X-ray (Förster Schreiber et al. 2019). High ionization lines, such as N V, Si IV, and C IV, that are indicative of AGN are also detected in the LRIS spectra. We find that 9 of the 12 galaxies identified as AGN based on characteristics from multi-wavelength data also have signatures of AGN in their LRIS spectra. The remaining 3 do not have emission of high ionization lines. In addition, we find 2 galaxies have AGN signatures in the LRIS spectra that were not previously identified as hosting AGN, yielding a total sample of 14 galaxies with AGN signatures. We have confirmed that the trends described in Section 4 are unaffected if we either include or exclude objects identified as AGN.

3.4. Composite Spectra

Out of our total of 80 usable spectra, there are only 57 that have at least one rest-UV feature measured in LRIS spectra. Limiting our sample to galaxies where only absorption lines or only Lyα are measured may bias our

results. To fold the full sample of 80 usable LRIS spectra, regardless of requiring significant detections of LIS or Lyα lines, we construct composite spectra of equal-number bins (26 or 27 galaxies per bin) according to different galactic properties. We use these composite spectra to evaluate the average outflow velocities within different bins of galaxy properties. To create the composite spectra, we shifted each individual flux-calibrated galaxy spectrum into the rest frame, interpolated the spectra onto a common wavelength grid, and calculated the median flux of the full bin at each wavelength. We measured Δv_LIS and $\Delta v_\text{Lyα}$ using the same methods as for individual spectra as described in Section 3.1.

4. RESULTS

In this section, we search for relations between outflow velocity and various galactic properties (i.e., inclination, SFR, Σ_SFR, M_*, and ΔMS). We also analyze the relationship between these galactic properties and LRIS and KMOS outflow detection fractions. We use galaxies presented in Table 3 for our analysis.

4.1. Inclination

4.1.1. Individual Measurements

In the nearby universe, it has been shown that galaxy outflows are collimated perpendicular to the disk, while inflows occur along the major axis of the galaxy (Heckman et al. 1990; Chen et al. 2010; Newman et al. 2012b; Concas et al. 2019; Roberts-Borsani & Saintonge 2019). Using 140,625 galaxies from SDSS with $0.05 \leq z \leq 0.18$, Chen et al. (2010) find that the outflow velocity is greater for more face-on galaxies, demonstrating that, in the local universe, galactic outflows are collimated. Furthermore, Bordoloi et al. (2011) investigate the Mg II absorption strength of low-redshift ($0.5 < z < 0.9$) galaxies and find that Mg II absorption is associated with bipolar regions aligned with the disk axis. This suggests that the model for collimated outflows holds true up to $z \sim 1$. Kornei et al. (2012) study 72 star-forming galaxies at $z \sim 1$ and find that face-on galaxies with lower inclination exhibit faster outflows compared to more edge-on galaxies with higher inclination. These results suggest that galactic winds also appear collimated for galaxies at $z \sim 1$. Similarly, Rubin et al. (2014) analyze 105 galaxies at $0.3 \leq z \leq 1.4$ and find that the outflow detection rate depends on inclination. They find that outflows are detected in $\sim 89\%$ of face-on galaxies ($i < 30°$) while outflows are only detected in $\sim 45\%$ of edge-on galaxies ($i > 50°$). Contrary to these well established findings in the local universe, the situation at higher redshift is less clear (Law et al. 2012; Newman et al. 2012b; Förster Schreiber et al. 2019; Wel-

---

[1] If one were to adopt a reasonable value for the finite intrinsic thickness (i.e., $\gamma = 0.2$, where γ is the ratio between the smallest and largest axes), at most, the difference would be ~ 7 degrees for the most highly inclined systems in our sample.

don et al. 2022). Most relevant to this analysis, in the
larger KMOS^{3D} parent sample, Förster Schreiber et al.
(2019) found no significant link between the frequency
of outflow detection and axis ratio (q) in their sample
of galaxies with $z \sim 0.6 - 2.7$.

As shown in Figure 3 and Table 5, we find that there is
no correlation between outflow velocity and inclination
in our sample. Furthermore, we find that there is no
relationship between the outflow detection rates of ei-
ther KMOS or LRIS and inclination. However, galaxies
that exhibit significant outflows from $\Delta v_{\rm LIS}$ with both
KMOS and LRIS appear to tend more toward higher
inclinations, meaning more edge-on galaxies.

4.1.2. *Inclination Stacks*

To further analyze how outflow velocity depends on
galaxy inclination, we split our sample into three equal-
number bins based on inclination. The composite spec-
tra, in order of increasing inclination, i, have $\langle i \rangle =
34°, 52,° 65°$ with 27, 27, and 26 galaxies in each stack
respectively (Figure 3). As shown in Figure 3, we find
no correlation between galaxy inclination and $\Delta v_{\rm LIS}$.

4.2. *Galaxy Stellar Properties*
4.2.1. *SFR*

A galaxy's SFR provides information on the amount
of mechanical energy and radiation pressure available for
driving outflows in star-forming galaxies. Several studies
have found that outflow velocities increase with increas-
ing SFR (Martin 2005; Rupke et al. 2005; Weiner et al.
2009; Bordoloi et al. 2014; Chisholm et al. 2015; Suga-
hara et al. 2017; Prusinski et al. 2021). The relation be-
tween outflow velocity and SFR can provide information
on the driving mechanisms of the outflows. Specifically,
if outflow velocity weakly depends on SFR, the outflow
velocity may be driven by mechanical energy from su-
pernovae or stellar winds (Heckman et al. 2000; Ferrara
& Ricotti 2006; Chen et al. 2010). If the outflow veloc-
ity is strongly dependent on SFR, the outflow velocity
may be radiatively driven (Sharma & Nath 2012). Many
other studies have failed to find such a correlation due
to a limited range in SFR available in their data (Steidel
et al. 2010; Kornei et al. 2012; Newman et al. 2012b).
Weldon et al. (2022) probe 155 galaxies with SFRs span-
ning $2 - 93 M_\odot {\rm yr}^{-1}$, and find an absence of correlation
between $\Delta v_{\rm LIS}$ and SFR. This suggests that $\Delta v_{\rm LIS}$ is
potentially influenced by the presence of stationary gas
near the systemic redshift of the galaxy. Furthermore,
they find there is a small correlation between $\Delta v_{\rm Ly\alpha}$ and
SFR, which indicates that galactic outflows are driven
by radiation pressure or supernova (Chevalier & Clegg
1985; Murray et al. 2011).

We find that there is no correlation between $\Delta v_{\rm LIS}$
and SFR in our sample as shown in Figure 4 and Table
5. Furthermore, our composite spectra (Figure 4) show
no trends between $\Delta v_{\rm LIS}$ and SFR.

4.2.2. *SFR Surface Density*

Environments with elevated $\Sigma_{\rm SFR}$ have a higher sur-
face density of radiation pressure, and the radiation
pressure acting on dust grains is more efficient. There-
fore, areas with high $\Sigma_{\rm SFR}$ may be more efficient at
transporting momentum and energy from overlapping
supernovae or stellar winds from massive stars into the
ISM (Veilleux et al. 2005). The combination of a higher
concentration of star formation, meaning more radiation
and higher density of SNe, along with efficient radia-
tive coupling, from high concentrations of dust, results
in conditions susceptible to launching outflows in high
$\Sigma_{\rm SFR}$ environments. In order for galaxies to sustain out-
flows, Heckman (2001) proposed that galaxies must ex-
ceed a $\Sigma_{\rm SFR}$ threshold of ~ 0.05 M$_\odot$ yr^{-1} kpc^{-2} for the
Chabrier (2003) IMF.

At $z \leq 1$, there is a relationship between $\Sigma_{\rm SFR}$ and
outflow velocity (Chen et al. 2010; Kornei et al. 2012;
Rubin et al. 2014; Chisholm et al. 2015). At higher red-
shift ($z > 1$), Newman et al. (2012b) found that the
relative strengths of the broad outflow and narrow star
formation components in rest-optical (Hα) line emission
showed the strongest difference with $\Sigma_{\rm SFR}$ among galaxy
properties (at 20σ between the low and high $\Sigma_{\rm SFR}$ bins);
a finer parameter space sampling showed a steep increase
around $\Sigma_{\rm SFR}$ of ~ 1 M$_\odot$ yr^{-1} kpc^{-2}, which could re-
flect the thicker, more turbulent gas-rich disks at ear-
lier epochs. In the large sample analyzed by Förster
Schreiber et al. (2019), the incidence of star formation-
driven outflows showed a smoother increase with the
fraction exceeding 15% at $\Sigma_{\rm SFR}$ of ~ 1 M$_\odot$ yr^{-1} kpc^{-2}.
Davies et al. (2019) exploited the high resolution of the
subset of SINS/zC-SINF sample observed with adaptive
optics to investigate trends of broad outflow emission
in Hα+[N II] by stacking spectra of spaxels ($\sim 1 - 2$
kpc scales) in bins of local physical properties across all
28 non-AGN galaxies, finding a consistent but some-
what lower threshold of $\Sigma_{\rm SFR} \sim 0.3 M_\odot {\rm yr}^{-1} {\rm kpc}^{-2}$,
and derived $v_{\rm out} \propto \Sigma_{\rm SFR}^{0.34}$, intermediate between
the shallow power-law for energy-driven winds (Chen
et al. 2010) and steeper power-law for momentum-driven
winds (e.g., Murray et al. 2011). In contrast, Steidel
et al. (2010) and Weldon et al. (2022) reported no corre-
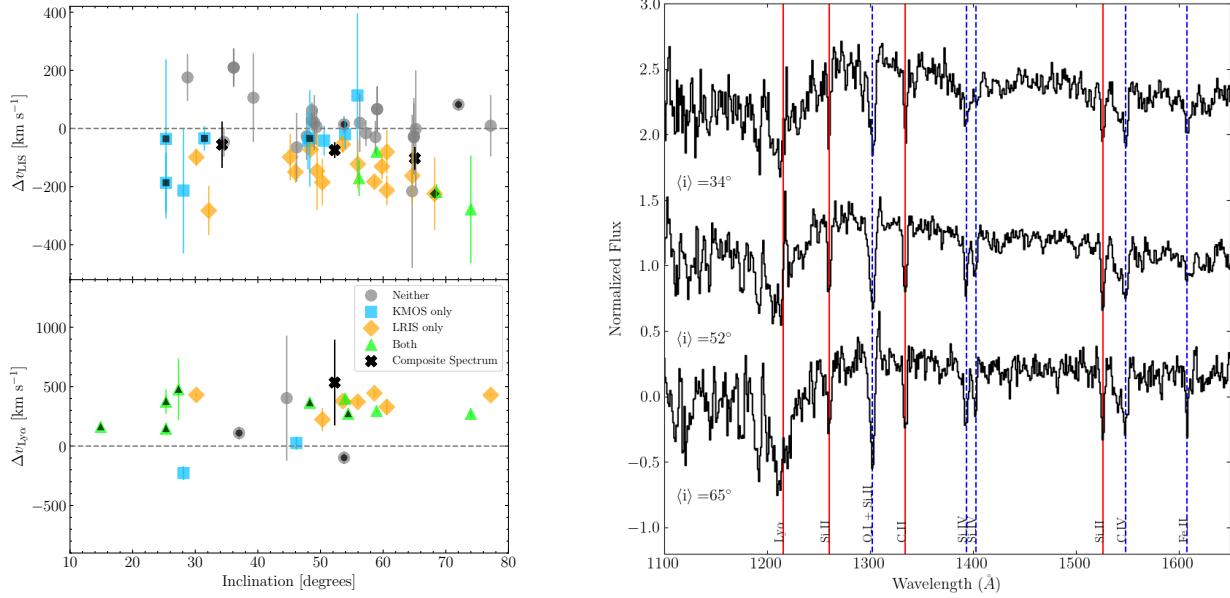
Figure 3. *Left:* Δv_{LIS} versus inclination (top) and $\Delta v_{\text{Ly}\alpha}$ versus inclination (bottom). Blue squares represent galaxies that had a significant outflow detection in KMOS, orange diamonds are for galaxies with a 1σ outflow detection in the LRIS sample, gray circles are galaxies that had no significant outflow detections, and green triangles are for galaxies where both KMOS and LRIS found significant outflows. Black "X" symbols represent the composite spectra. In the bottom panel, there is only one composite spectrum data point, as Lyα emission was only detected in one of the three composite spectra. Data points with black markers inside indicate galaxies identified as hosting AGN. *Right:* Composite spectra for three inclination bins. The top is the composite spectrum for our low inclination sample with $\langle i \rangle = 34°$ (27 galaxies). The middle is the composite spectrum for our mid inclination sample with $\langle i \rangle = 52°$ (27 galaxies). The bottom is the composite spectrum for our high inclination sample with $\langle i \rangle = 65°$ (26 galaxies). The laboratory wavelengths for Lyα and the absorption lines are plotted as vertical lines. Red lines indicate the lines used for our analysis while blue dotted lines are other features present in the spectra.

Table 5. Correlation coefficients between outflow and galaxy properties

Galaxy Property	$\rho_{\Delta v_{\text{LIS}}}$	$\rho_{\Delta v_{\text{Ly}\alpha}}$	$\rho_{v_{\text{max}}}$
i	$-0.17(0.245)$	$0.26(0.261)$	$-0.04(0.810)$
log(SFR)	$0.04(0.784)$	$0.15(0.511)$	$-0.44(0.002)$
log(Σ_{SFR})	$-0.1(0.502)$	$0.20(0.397)$	$-0.15(0.291)$
log(M$_*$)	$-0.07(0.612)$	$-0.29(0.200)$	$-0.17(0.234)$
ΔMS	$0.13(0.349)$	$0.44(0.044)$	$-0.27(0.056)$

[*]Each column lists the correlation coefficient ρ (with corresponding p-values in parentheses), between Δv_{LIS}, $\Delta v_{\text{Ly}\alpha}$, or v_{max} and one of several stellar properties.
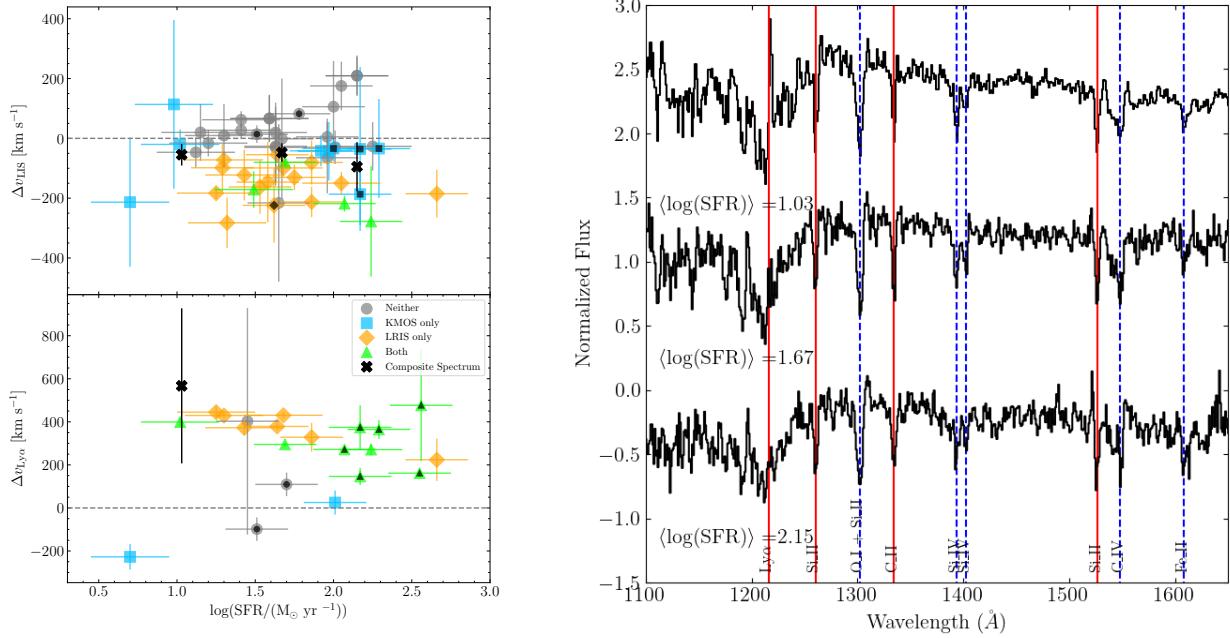
Figure 4. *Left:* Same as Figure 3 but for Δv_{LIS} vs log(SFR) (top) and $\Delta v_{\mathrm{Ly}\alpha}$ vs log(SFR) (bottom). In the bottom panel, there is only one composite spectrum data point, as Lyα emission was only detected in one of the three composite spectra. *Right:* The same as Figure 3, but for three log(SFR) bins. The top is the composite spectrum for our low inclination sample with $\langle\log(\mathrm{SFR})\rangle = 1.03$ (27 galaxies). The middle is the composite spectrum for our mid inclination sample with $\langle\log(\mathrm{SFR})\rangle = 1.67$ (27 galaxies). The bottom is the composite spectrum for our high inclination sample with $\langle\log(\mathrm{SFR})\rangle = 2.15$ (26 galaxies).

Table 6. Mean values for several star properties for different outflow detection methods

Outflow Detection	$\langle\log(\mathrm{SFR/M_\odot\ yr^{-1}})\rangle$	$\langle\log(\Sigma_{\mathrm{SFR}}/\mathrm{M_\odot yr^{-1}kpc^{-2}})\rangle$	$\langle\log(\mathrm{M_*/M_\odot})\rangle$	$\langle\Delta\mathrm{MS}\rangle$	$\langle\mathrm{i}\rangle$ (deg)
Neither	1.14 ± 0.10	-0.26 ± 0.08	10.35 ± 0.04	-0.20 ± 0.10	51 ± 2.9
KMOS Only	1.91 ± 0.11	0.10 ± 0.14	10.74 ± 0.09	0.03 ± 0.10	50 ± 2.6
LRIS Only	1.63 ± 0.08	0.06 ± 0.11	10.23 ± 0.08	0.06 ± 0.08	52 ± 2.8
Both	2.03 ± 0.13	0.82 ± 0.23	10.59 ± 0.14	0.12 ± 0.07	46 ± 5.7

lation between outflow velocity and Σ_{SFR}. Weldon et al. (2022) suggest the absence of observed correlation may stem from challenges in pinpointing the actual location of the gas and its coupling to star formation activity. This discrepancy could be exacerbated by potential limitations in LRIS observations, and the relationship may remain elusive due to its weak nature within constrained dynamical ranges of Σ_{SFR}.

As shown in Figure 5 and Table 5, we find no significant trends between outflow velocity and Σ_{SFR} in our sample. Furthermore, our composite spectra (Figure 5) also show no trends between outflow velocity and Σ_{SFR}.

4.2.3. *Stellar Mass*

Galaxies with a lower stellar mass (M_*) have a lower gravitational potential, resulting in a more efficient launch of outflows (Reddy et al. 2022). Our KMOS[3D] parent sample from Förster Schreiber et al. (2019), show that SF-driven winds show no significant dependence on stellar mass. For galaxies with a stellar mass at $\log(M_*/M_\odot) \geq 10.3$, SF-driven winds may not escape the galaxy but instead contribute to driving fountains (Dekel & Silk 1986; Murray et al. 2005; Oppenheimer & Davé 2008; Übler et al. 2014). Martin et al. (2012), found that the detection rate of outflows does not rely on stellar mass. Additionally, Heckman & Borthakur (2016) and Prusinski et al. (2021) find no correlation between stellar mass and outflow velocity. Förster Schreiber et al. (2019) also find that the incidence, strength, and velocity of AGN-driven outflows are dependent on stellar mass, with most AGN-driven outflows detected above $\log(M_*/M_\odot) = 10.7$.

Drawing from the same KMOS[3D] sample as Förster Schreiber et al. (2019), we find that there is no correlation between outflow velocity and M_* (Figure 6 and Table 5). Figure 6 also illustrates that the composite spectra show no correlation as well. Furthermore, we find no correlation between outflow velocity and the method in which the outflow was detected (Table 6).

4.2.4. *ΔMS*

Using the KMOS[3D] sample, Förster Schreiber et al. (2019) find that AGN-driven outflows are not correlated with ΔMS while SF-driven outflows are detected at higher ΔMS. At $\Delta MS \geq +0.6$ dex, they find the highest percentage ($25 - 30\%$) of detected SF-outflows. These "starbursting outliers" drive a SF-driven outflow that is detectable in the rest-optical line emission (Rodighiero et al. 2011; Förster Schreiber et al. 2019).

As shown in Figure 7 and Table 5, there is no correlation between Δv_{LIS} and ΔMS among galaxies in our sample. While Table 5 suggests there may be a relationship between $\Delta v_{\mathrm{Ly\alpha}}$ and ΔMS, ($p = 0.044$), the sample

size is small with only 12 galaxies being included. Therefore, a larger sample is needed to robustly probe this relation. Figure 7 also illustrates that the composite spectra show no correlation.

4.3. *Maximum Outflow Velocity*

In addition to analyzing the relationships between Δv_{LIS} and the various stellar properties, we test if the stellar properties are correlated with v_{max}. As shown in Figure 8 and Table 5, our results for inclination, Σ_{SFR}, M_*, and ΔMS are qualitatively unchanged compared to our v_{LIS} results. However, we find a statistically significant correlation between v_{max} and SFR. Our results show that galaxies with a higher SFR have a higher maximum outflow velocity. These results agree with Weldon et al. (2022) and support the idea that supernova or radiation pressure drive galactic outflows (Chevalier & Clegg 1985; Murray et al. 2011). Given this strong correlation, v_{max} might be a more reliable measure of the correlations between outflow velocity and other galactic stellar properties.

4.4. *Average Galaxy Properties of Outflow Samples*

While we do not observe strong correlations between outflow and galaxies properties in the scatter plots or stacked spectra, we do find a relationship within the distinct stellar population properties (SFR, Σ_{SFR}, and ΔMS) when looking at the stellar property distributions of the different outflow detections (Figure 9 and Table 6). We find that the average SFR, Σ_{SFR}, and ΔMS are significantly higher in cases where outflows are detected than when they are not detected. Table 6 shows that the highest averages are for cases when outflows are detected in both KMOS and LRIS for SFR, Σ_{SFR}, and ΔMS. This result provides evidence that there is a connection between outflow and galaxy properties given that the mean star formation properties of the outflow samples are higher than the mean properties of the non-outflow samples. Figures 4, 5, 7 show no significant trends with outflow speed, suggesting that these correlations are noisy.

To test these correlations, we performed jackknife simulations by pulling 80 random galaxies from the parent KMOS[3D] sample within the same redshift range as our LRIS sample to create 1000 mock samples. We split these mock samples into 3 bins based on the stellar properties, and found the average detection fraction for each bin. Our simulations recover trends consistent with our LRIS sample with large uncertainties (Figure 10), suggesting that a larger sample (i.e, a sample twice as large) spanning a wider dynamic range in galaxy properties is required.
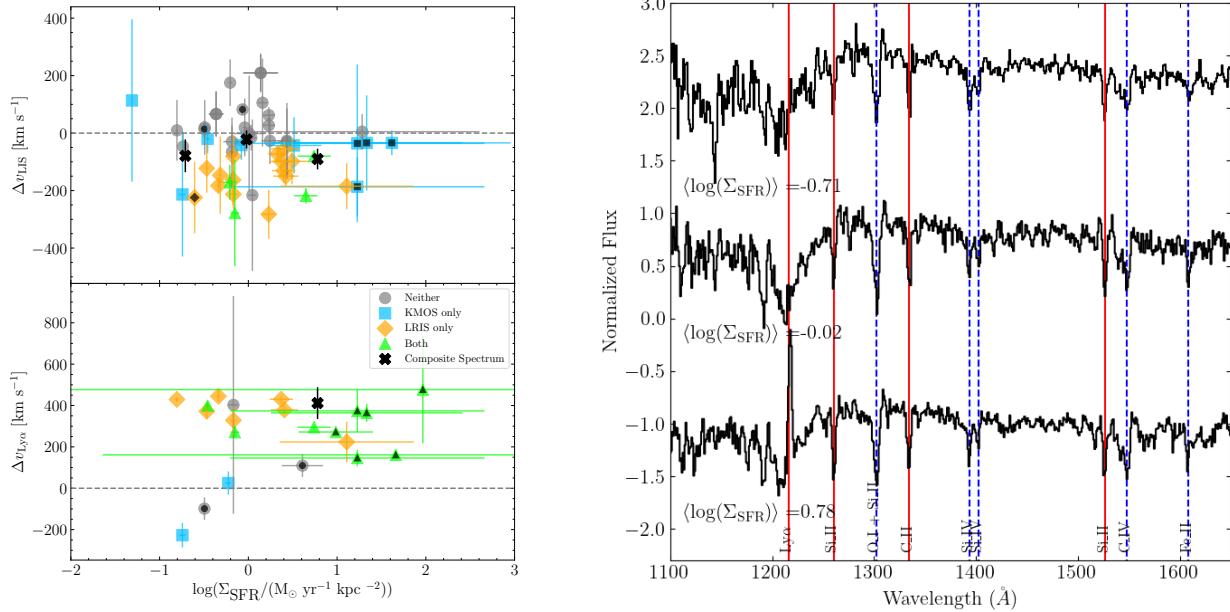
Figure 5. *Left:* Same as Figure 3 but for Δv_{LIS} vs $\log(\Sigma_{\mathrm{SFR}})$ (top) and $\Delta v_{\mathrm{Ly}\alpha}$ vs $\log(\Sigma_{\mathrm{SFR}})$(bottom). In the bottom panel, there is only one composite spectrum data point, as Lyα emission was only detected in one of the three composite spectra. *Right:* The same as Figure 3, but for three $\log(\Sigma_{\mathrm{SFR}})$ bins. The top is the composite spectrum for our low inclination sample with $\langle\log(\Sigma_{\mathrm{SFR}})\rangle = -0.71$ (27 galaxies). The middle is the composite spectrum for our mid inclination sample with $\langle\log(\Sigma_{\mathrm{SFR}})\rangle = -0.02$ (27 galaxies). The bottom is the composite spectrum for our high inclination sample with $\langle\log(\Sigma_{\mathrm{SFR}})\rangle = 0.78$ (26 galaxies).

Higher SFR, Σ_{SFR}, and ΔMS in galaxies with detected outflows also suggest that outflows may only be launched and detectable above some threshold of SFR, Σ_{SFR}, and ΔMS (McKee & Ostriker 1977; Heckman 2002; Rubin et al. 2014; Chisholm et al. 2015; Roberts-Borsani et al. 2020; Weldon et al. 2022). This is possible if the maximum outflow velocity that can be produced from star formation alone has an Eddington limit (Murray et al. 2005; Thompson et al. 2005; Hopkins et al. 2010), or if the outflow speed is modulated by the density of the surrounding ISM.

5. DISCUSSION

5.1. *Outflow Kinematics*

As shown in Figure 2, we find that $\langle\Delta v_{\mathrm{LIS}}\rangle = -56 \pm 16$ km s^{-1} and $\langle\Delta v_{\mathrm{Ly}\alpha}\rangle = 266\pm41$km s^{-1}. Steidel et al. (2010) use a similar sample to ours (i.e., 89 galaxies at $2 \leq z \leq 3$) to quantify a galaxy outflow velocities using interstellar absorption lines (IS) (C II λ1334, Si IV λ1393, Si II λ1526) and Lyα. These authors find $\langle\Delta v_{\mathrm{IS}}\rangle = -164\pm16$km s^{-1} and $\langle\Delta v_{\mathrm{Ly}\alpha}\rangle = 445\pm27$km s^{-1}, which are significantly more offset from zero than our results.

Although Steidel et al. (2010) do not report error bars on outflow velocities, we can look at the general shape of the Δv_{LIS} and $\Delta v_{\mathrm{Ly}\alpha}$ histograms to analyze the differences in our average outflow velocities. Steidel et al. (2010) find 11 out of their 89 galaxies to have $\Delta v_{\mathrm{IS}} \geq 0$. Moreover, all of their $\Delta v_{\mathrm{IS}} \leq +100$ km s^{-1}. We find 15 out of 80 galaxies in our sample have $\Delta v_{\mathrm{LIS}} \geq 0$ with 5 galaxies having $\Delta v_{\mathrm{LIS}} \geq 100$ km s^{-1}. Furthermore, Steidel et al. (2010) find no Lyα measurements that are bluer than 100 km s^{-1}, whereas we find 3 galaxies measurements in the $v_{\mathrm{Ly}\alpha} < 0$ regime (Figure 2).

One source for these discrepancies may be the sample selection criteria. Although both Steidel et al. (2010) and our sample investigate main sequence star-forming galaxies, we select our samples differently. Most notably, Steidel et al. (2010) select galaxies in the rest-UV down to a fixed rest UV luminosity with a median absolute UV magnitude of $M_{UV} = -20.42$, while our parent sample, KMOS[3D] from Förster Schreiber et al. (2019), was selected down to fixed rest-optical luminosity with a median absolute UV magnitude of $M_{UV} = -19.93$, 0.5 magnitudes fainter in the rest-UV. These differences sample UV continuum luminosity selection may translate into differences in the properties of gas flows probed, but a detailed sample comparison is outside the scope of this work.
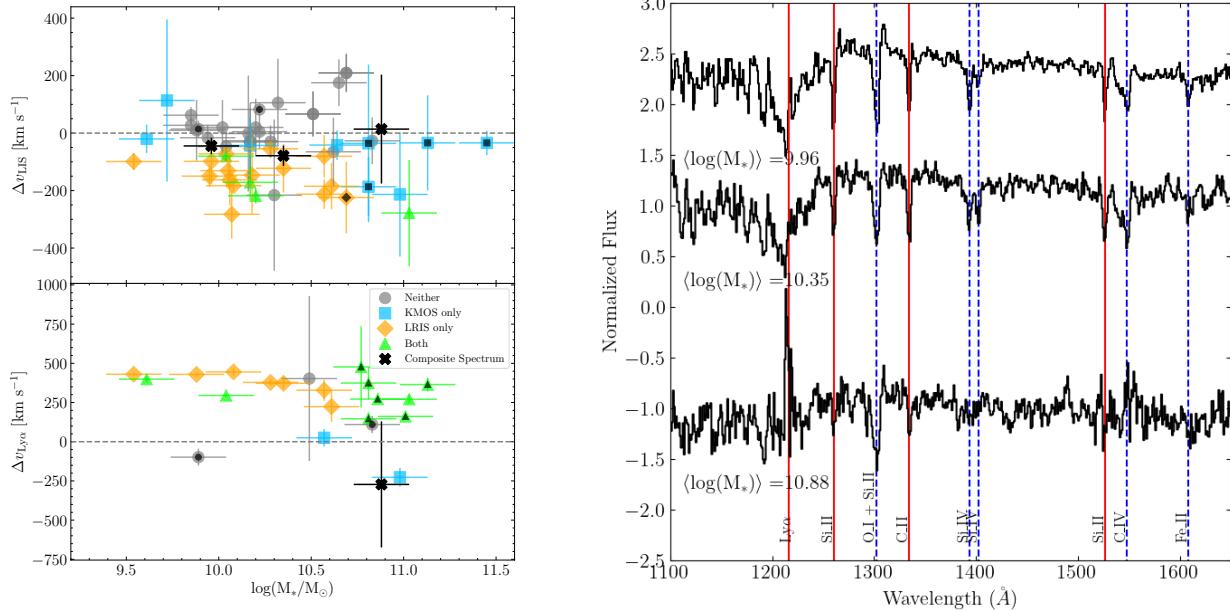
Figure 6. *Left:* Same as Figure 3 but for $\Delta v_{\rm LIS}$ vs $\log(M_*)$ (top) and $\Delta v_{\rm Ly\alpha}$ vs $\log(M_*)$ (bottom). In the bottom panel, there is only one composite spectrum data point, as Lyα emission was only detected in one of the three composite spectra. *Right:* The same as Figure 3, but for three M_* bins. The top is the composite spectrum for our low inclination sample with $\langle M_* \rangle = 9.96$ (27 galaxies). The middle is the composite spectrum for our mid inclination sample with $\langle M_* \rangle = 10.35$ (27 galaxies). The bottom is the composite spectrum for our high inclination sample with $\langle M_* \rangle = 10.88$ (26 galaxies).

We find that our results are in agreement with other work that show lower velocities than those reported in Steidel et al. (2010). For example, Weldon et al. (2022) use the MOSDEF-LRIS survey and measured $\Delta v_{\rm LIS}$ and $\Delta v_{\rm Ly\alpha}$ for 155 star forming galaxies at $1.42 \le z \le 3.48$. A small overlap exists in our samples since we include 22 galaxies from the MOSDEF-LRIS survey, yet the samples are largely independent. In the MOSDEF-LRIS sample, they found that the peak distribution for $\Delta v_{\rm LIS}$ was -60 km s^{-1}. Furthermore, as in our sample, there are several galaxies with $\Delta v_{\rm Ly\alpha} < 100$ km s^{-1}. Talia et al. (2012) and Calabrò et al. (2022) also present results consistent with those presented here. Talia et al. (2012) used 74 rest-frame UV spectra from the Galaxy Mass Assembly ultra-deep Spectroscopic Survey (GMASS) with a redshift range of $1.5 \le z \le 2.8$. They used composite spectra to calculate the velocities of the strongest interstellar absorption lines (a mixture of low and high ionization lines denoted as $\Delta v_{\rm IS}$) and found the average $\Delta v_{\rm IS} \sim -100$ km s^{-1}. Calabrò et al. (2022) study 330 galaxies at $2 \le z \le 4.6$ using the VANDELS survey and find the average velocity traced by UV absorption lines was $\Delta v_{\rm IS} = -60 \pm 10$ km s^{-1}. Furthermore, they report a positive velocity shift for 39% of their sample.

These results present outflows with velocities closer to zero, suggesting a more nuanced picture (Steidel et al. 2010). The smaller velocities may imply that there is greater absorption at the galaxies systemic redshift that is more prominent in $z \sim 2$ galaxies. A more thorough decomposition of the absorption line may be necessary, separating the component associated with the galaxy disk from the one associated with an outflow (Weiner et al. 2009; Steidel et al. 2010; Martin et al. 2012; Rubin et al. 2014). Furthermore, we find that the Lyα kinematics are more complex given that there is evidence of blueshifted gas in the Lyα, which is indicative of infalling gas (Verhamme et al. 2006; Kulas et al. 2012; Weldon et al. 2023).

5.2. *Inferred Geometry*

Our results show no strong correlation with inclination implying the outflows are not collimated (Figure 3). Outflows with a spherical geometry and unity covering fraction would have a $\sim 100\%$ detection rate. However, we find outflows detected with KMOS have a 30% detection rate while outflows detected with LRIS have a 49% detection rate. KMOS outflows are detected with Hα kinematics while LRIS outflow detections are found with LIS absorption lines and Lyα emission. The lower
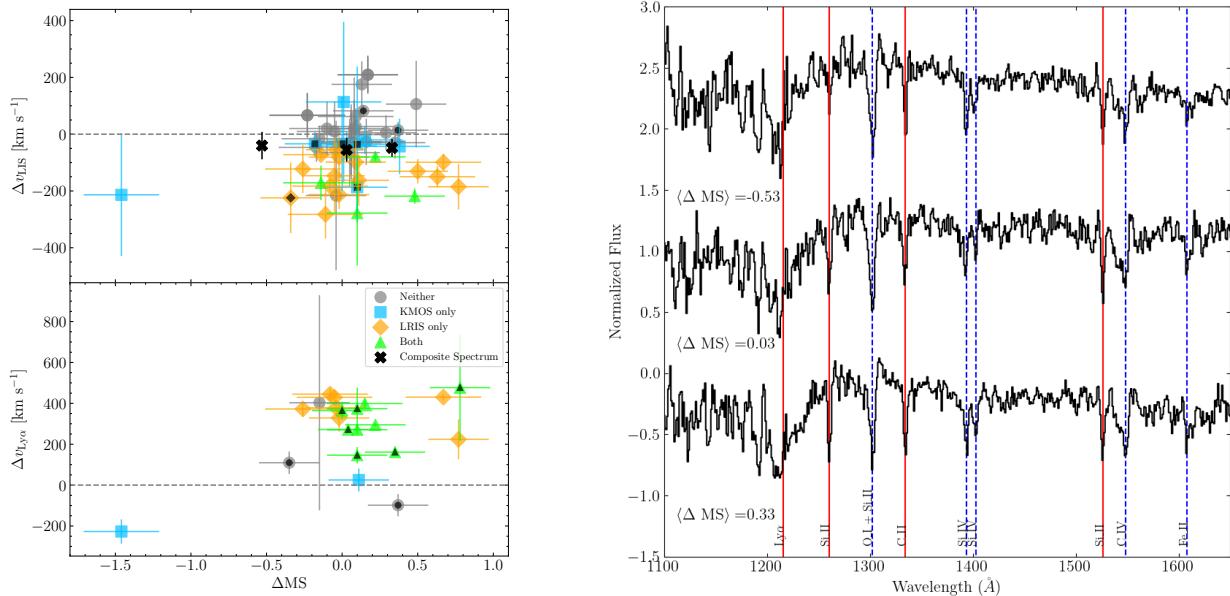
Figure 7. *Left:* Same as Figure 3 but for Δv_{LIS} vs ΔMS (top) and $\Delta v_{\mathrm{Ly}\alpha}$ vs ΔMS (bottom). In the bottom panel, there are no composite spectra data points, as Lyα emission was not detected in any of the three composite spectra. *Right:* The same as Figure 3, but for three ΔMS bins. The top is the composite spectrum for our low inclination sample with $\langle\Delta$MS$\rangle = -0.53$ (27 galaxies). The middle is the composite spectrum for our mid inclination sample with $\langle\Delta$MS$\rangle = 0.03$ (27 galaxies). The bottom is the composite spectrum for our high inclination sample with $\langle\Delta$MS$\rangle = 0.33$ (26 galaxies).
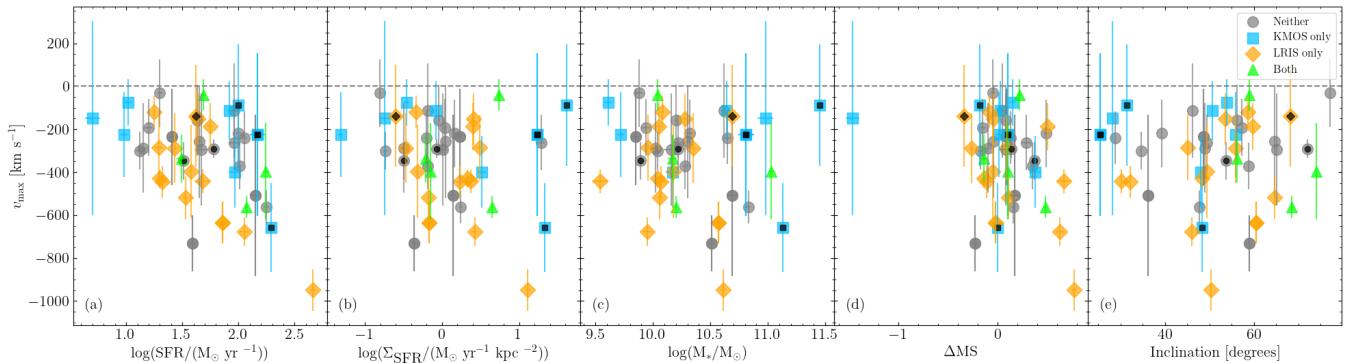
Figure 8. Relationships between $v_{\max}$ and the various galaxy properties. Grey circles indicate galaxies without significant outflow detections, blue squares indicate galaxies with a significant outflow detection in KMOS, orange diamonds indicate galaxies with a 1σ outflow detection in the LRIS sample, and green triangles indicate galaxies where significant outflows were detected in both KMOS and LRIS. Relationships for *(a):* SFR; *(b):* Σ_{SFR}; *(c):* M$_*$; *(d):* ΔMS; *(e):* inclination.

detection rate for KMOS Hα outflows implies that Hα may be more sparsely distributed with lower covering fraction while neutral outflow gas traced from LIS absorption lines covers a larger solid angle surrounding the galaxy. Moreover, these tracers might exhibit sensitivity to varying timescales of outflow activity. For instance, Hα provides a more instantaneous insight as it explores material closer to the launching site of outflows. In con-

trast, rest-UV lines could be dispersed across greater distances and lower densities along the line of sight. In future work, we will analyze the geometry of outflows more closely with JWST images in the COSMOS and GOODS-S fields. Furthermore, as in previous work (e.g., Steidel et al. (2010); Weldon et al. (2022)), we find that the connections between outflow and galaxy properties are noisy with our small dynamic range. A larger sam-
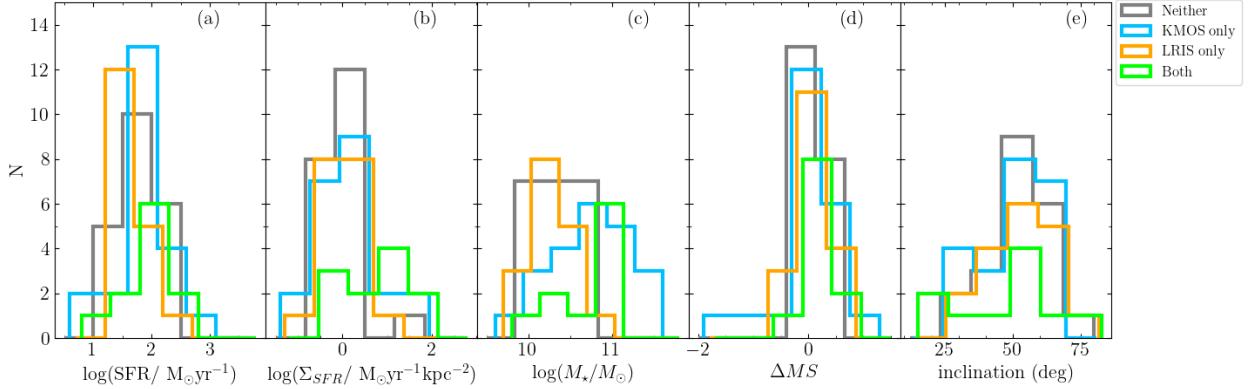
Figure 9. Distributions of stellar properties with different outflow detections. The blue bars represent galaxies with outflows detected with only KMOS (Förster Schreiber et al. 2019), orange bars represent galaxies with outflows detected with LRIS only, and green bars represent galaxies with outflows detected from both KMOS and LRIS. Distributions of *(a):* SFR; *(b):* $\Sigma_{\rm SFR}$; *(c):* M_*; *(d):* ΔMS; *(e):* inclination.
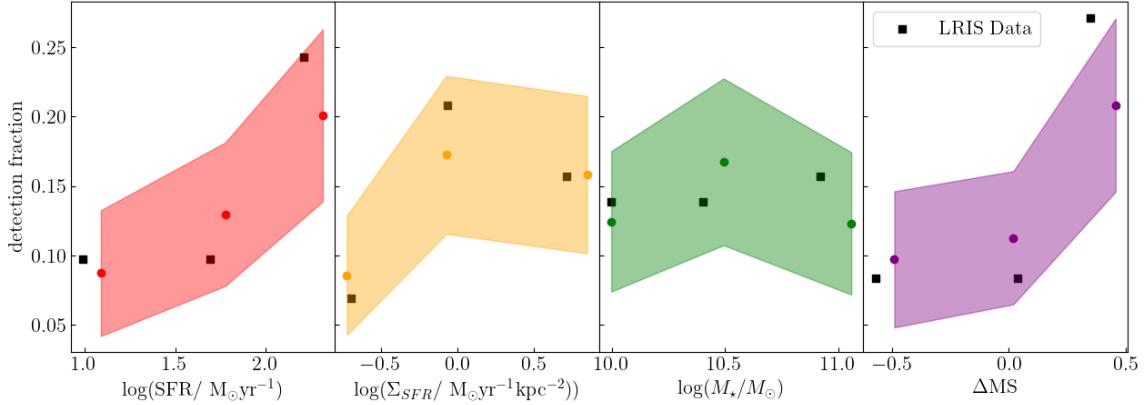
Figure 10. Results from 1000 realizations of entire KMOS-LRIS-size samples drawn from the entire KMOS$^{\rm 3D}$ sample. Each simulation drew 80 galaxies at $z = 1.4 - 2.7$ from the 600 galaxy parent sample and separated the galaxies into 3 bins based on the stellar properties. The bins contain 27, 27, and 26 galaxies, respectively. The colored data points represent the average values found from the simulations, the shaded regions represent the uncertainty, and the black squares are the averages found from our LRIS sample.

ple is needed with a wide enough dynamic range to robustly probe these relations. In addition, larger samples resolved on sub-galactic scales (e.g., expanding previous studies with AO-assisted IFU of star-forming galaxies and/or strongly lensed sources), will aid by enabling a more direct association of the local stellar properties and outflow launching sites and potential provide better constraints on outflow geometry.

6. CONCLUSIONS

We utilized a sample of 80 galaxies with a redshift range of $1.4 \le z \le 2.7$ to investigate galaxy outflows. To explore the multi-phase nature of galaxy outflows, we use a novel data set that includes both LRIS and KMOS in order to probe galaxy outflows in both Hα

and the rest-UV. Outflows are identified in galaxies by using broad Hα (+[N II]+[S II]) emission or by identifying low ionization interstellar absorption lines or Lyα emission. Outflow velocities are measured from rest-UV features. We also examine how outflow velocity depends on various galactic properties such as SFR, $\Sigma_{\rm SFR}$, M_*, ΔMS, and inclination. Our key results are as follows:

1. The mean velocities of our sample are $\langle \Delta v_{\rm LIS} \rangle = -56 \pm 16$ km s^{-1} and $\langle \Delta v_{\rm Ly\alpha} \rangle = 266 \pm 41$ km s^{-1}. These average velocities, lower than those found in previous work at a similar redshift range, suggest that the interstellar absorption lines have a multi-component structure (i.e., one component

from the galaxy disk and one component from the galaxy outflow).

2. In our sample, we find no significant correlation between outflow velocity from absorption line centroids and galaxy properties. However, we find that the average SFR, Σ_{SFR}, and ΔMS are significantly higher in galaxies where outflows are detected, reflecting underlying trends in incidence of outflow detection reported for larger samples, such as the parent sample of 599 SFGs (Förster Schreiber et al. 2019). In addition, we find that quantifying outflow kinematics in terms of the maximum outflow velocity, v_{max}, may be more sensitive to underlying correlations.

3. Outflow velocity is not correlated with inclination, implying that outflows are not collimated. Furthermore, we did not have a 100% detection rate meaning outflows cannot be spherical either. These two results suggest that outflows are sparsely distributed. We find that outflows detected with Hα have a 30% detection rate while galaxies detected with LIS absorption lines have a 49% detection rate meaning that LIS absorption lines cover a larger solid angle. Furthermore, LIS absorption lines trace longer scales and lower densities along the line of sight of outflow activity compared to Hα.

We find that the correlations between outflow properties and galaxy properties have a significant amount of intrinsic scatter. Thus, a larger sample with a wider dynamic range and a a sample that explores these correlations on spatially-resolved scales are needed to better understand these relationships. Furthermore, higher resolution rest-optical imaging from JWST will enable a more robust exploration of the geometry of galactic outflows. A full analysis of such observations will be crucial for a full understanding of outflows.

REFERENCES

Beckmann, R. S., Devriendt, J., Slyz, A., et al. 2017, MNRAS, 472, 949, doi: 10.1093/mnras/stx1831

Behroozi, P. S., Wechsler, R. H., & Conroy, C. 2013, ApJ, 770, 57, doi: 10.1088/0004-637X/770/1/57

Bordoloi, R., Lilly, S. J., Knobel, C., et al. 2011, ApJ, 743, 10, doi: 10.1088/0004-637X/743/1/10

Bordoloi, R., Lilly, S. J., Hardmeier, E., et al. 2014, ApJ, 794, 130, doi: 10.1088/0004-637X/794/2/130

Brusa, M., Bongiorno, A., Cresci, G., et al. 2015, MNRAS, 446, 2394, doi: 10.1093/mnras/stu2117

Bruzual, G., & Charlot, S. 2003, MNRAS, 344, 1000, doi: 10.1046/j.1365-8711.2003.06897.x

Calabrò, A., Amorín, R., Fontana, A., et al. 2017, A&A, 601, A95, doi: 10.1051/0004-6361/201629762

Calabrò, A., Pentericci, L., Talia, M., et al. 2022, A&A, 667, A117, doi: 10.1051/0004-6361/202244364

Calzetti, D., Armus, L., Bohlin, R. C., et al. 2000, ApJ, 533, 682, doi: 10.1086/308692

Cano-Díaz, M., Sánchez, S. F., Zibetti, S., et al. 2016, ApJL, 821, L26, doi: 10.3847/2041-8205/821/2/L26

Chabrier, G. 2003, PASP, 115, 763, doi: 10.1086/376392

Chen, Y.-M., Tremonti, C. A., Heckman, T. M., et al. 2010, AJ, 140, 445, doi: 10.1088/0004-6256/140/2/445

Chevalier, R. A., & Clegg, A. W. 1985, Nature, 317, 44, doi: 10.1038/317044a0

Chisholm, J., Tremonti, C. A., Leitherer, C., & Chen, Y. 2017, Monthly Notices of the Royal Astronomical Society, 469, 4831, doi: 10.1093/mnras/stx1164

Chisholm, J., Tremonti, C. A., Leitherer, C., et al. 2015, ApJ, 811, 149, doi: 10.1088/0004-637X/811/2/149

Concas, A., Popesso, P., Brusa, M., Mainieri, V., & Thomas, D. 2019, A&A, 622, A188, doi: 10.1051/0004-6361/201732152

Concas, A., Maiolino, R., Curti, M., et al. 2022, MNRAS, 513, 2535, doi: 10.1093/mnras/stac1026

Cresci, G., Mainieri, V., Brusa, M., et al. 2015, ApJ, 799, 82, doi: 10.1088/0004-637X/799/1/82

Croton, D. J., Springel, V., White, S. D. M., et al. 2006, MNRAS, 365, 11, doi: 10.1111/j.1365-2966.2005.09675.x

Dalcanton, J. J. 2007, ApJ, 658, 941, doi: 10.1086/508913

Davé, R., Finlator, K., & Oppenheimer, B. D. 2011, MNRAS, 416, 1354, doi: 10.1111/j.1365-2966.2011.19132.x

—. 2012, MNRAS, 421, 98, doi: 10.1111/j.1365-2966.2011.20148.x

Davies, R. L., Förster Schreiber, N. M., Übler, H., et al. 2019, ApJ, 873, 122, doi: 10.3847/1538-4357/ab06f1

Davies, R. L., Förster Schreiber, N. M., Lutz, D., et al. 2020, ApJ, 894, 28, doi: 10.3847/1538-4357/ab86ad

Dekel, A., & Silk, J. 1986, ApJ, 303, 39,
doi: 10.1086/164050

Di Matteo, T., Springel, V., & Hernquist, L. 2005, Nature,
433, 604, doi: 10.1038/nature03335

Erb, D. K. 2015, Nature, 523, 169,
doi: 10.1038/nature14454

Ferrara, A., & Ricotti, M. 2006, Monthly Notices of the
Royal Astronomical Society, 373, 571,
doi: 10.1111/j.1365-2966.2006.10978.x

Finlator, K., & Davé, R. 2008, MNRAS, 385, 2181,
doi: 10.1111/j.1365-2966.2008.12991.x

Fontanot, F., Calabrò, A., Talia, M., et al. 2021, MNRAS,
504, 4481, doi: 10.1093/mnras/stab1213

Förster Schreiber, N. M., Genzel, R., Newman, S. F., et al.
2014, ApJ, 787, 38, doi: 10.1088/0004-637X/787/1/38

Freeman, W. R., Siana, B., Kriek, M., et al. 2019, ApJ,
873, 102, doi: 10.3847/1538-4357/ab0655

Förster Schreiber, N. M., Übler, H., Davies, R. L., et al.
2019, The Astrophysical Journal, 875, 21,
doi: 10.3847/1538-4357/ab0ca2

Genzel, R., Newman, S., Jones, T., et al. 2011, ApJ, 733,
101, doi: 10.1088/0004-637X/733/2/101

Genzel, R., Tacconi, L. J., Kurk, J., et al. 2013, ApJ, 773,
68, doi: 10.1088/0004-637X/773/1/68

Genzel, R., Förster Schreiber, N. M., Lang, P., et al. 2014,
ApJ, 785, 75, doi: 10.1088/0004-637X/785/1/75

Harrison, C. M., Alexander, D. M., Mullaney, J. R., et al.
2016, MNRAS, 456, 1195, doi: 10.1093/mnras/stv2727

Heckman, T. M. 2001, Galactic Superwinds Circa 2001.
https://arxiv.org/abs/astro-ph/0107438

Heckman, T. M. 2002, in Astronomical Society of the
Pacific Conference Series, Vol. 254, Extragalactic Gas at
Low Redshift, ed. J. S. Mulchaey & J. T. Stocke, 292,
doi: 10.48550/arXiv.astro-ph/0107438

Heckman, T. M., Armus, L., & Miley, G. K. 1990, ApJS,
74, 833, doi: 10.1086/191522

Heckman, T. M., & Borthakur, S. 2016, ApJ, 822, 9,
doi: 10.3847/0004-637X/822/1/9

Heckman, T. M., Lehnert, M. D., Strickland, D. K., &
Armus, L. 2000, The Astrophysical Journal Supplement
Series, 129, 493, doi: 10.1086/313421

Hirschmann, M., Naab, T., Davé, R., et al. 2013, MNRAS,
436, 2929, doi: 10.1093/mnras/stt1770

Hopkins, P. F., Murray, N., Quataert, E., & Thompson,
T. A. 2010, MNRAS, 401, L19,
doi: 10.1111/j.1745-3933.2009.00777.x

Hopkins, P. F., Quataert, E., & Murray, N. 2012, Monthly
Notices of the Royal Astronomical Society, 421, 3522,
doi: 10.1111/j.1365-2966.2012.20593.x

Kornei, K. A., Shapley, A. E., Martin, C. L., et al. 2012,
ApJ, 758, 135, doi: 10.1088/0004-637X/758/2/135

Kriek, M., van Dokkum, P. G., Franx, M., et al. 2007, ApJ,
669, 776, doi: 10.1086/520789

—. 2008, ApJ, 677, 219, doi: 10.1086/528945

Kriek, M., Shapley, A. E., Reddy, N. A., et al. 2015, ApJS,
218, 15, doi: 10.1088/0067-0049/218/2/15

Kulas, K. R., Shapley, A. E., Kollmeier, J. A., et al. 2012,
ApJ, 745, 33, doi: 10.1088/0004-637X/745/1/33

Lang, P., Wuyts, S., Somerville, R. S., et al. 2014, ApJ,
788, 11, doi: 10.1088/0004-637X/788/1/11

Law, D. R., Steidel, C. C., Shapley, A. E., et al. 2012, ApJ,
759, 29, doi: 10.1088/0004-637X/759/1/29

Leung, G. C. K., Coil, A. L., Azadi, M., et al. 2017, ApJ,
849, 48, doi: 10.3847/1538-4357/aa9024

Leung, G. C. K., Coil, A. L., Aird, J., et al. 2019, ApJ, 886,
11, doi: 10.3847/1538-4357/ab4a7c

Madau, P., Ferguson, H. C., Dickinson, M. E., et al. 1996,
MNRAS, 283, 1388, doi: 10.1093/mnras/283.4.1388

Mannucci, F., Cresci, G., Maiolino, R., Marconi, A., &
Gnerucci, A. 2010, MNRAS, 408, 2115,
doi: 10.1111/j.1365-2966.2010.17291.x

Martin, C. L. 2005, ApJ, 621, 227, doi: 10.1086/427277

Martin, C. L., Shapley, A. E., Coil, A. L., et al. 2012, ApJ,
760, 127, doi: 10.1088/0004-637X/760/2/127

McKee, C. F., & Ostriker, J. P. 1977, ApJ, 218, 148,
doi: 10.1086/155667

Momcheva, I. G., Brammer, G. B., van Dokkum, P. G.,
et al. 2016, ApJS, 225, 27,
doi: 10.3847/0067-0049/225/2/27

Moster, B. P., Somerville, R. S., Maulbetsch, C., et al.
2010, ApJ, 710, 903, doi: 10.1088/0004-637X/710/2/903

Murray, N., Ménard, B., & Thompson, T. A. 2011, ApJ,
735, 66, doi: 10.1088/0004-637X/735/1/66

Murray, N., Quataert, E., & Thompson, T. A. 2005, ApJ,
618, 569, doi: 10.1086/426067

Newman, S. F., Shapiro Griffin, K., Genzel, R., et al.
2012a, ApJ, 752, 111, doi: 10.1088/0004-637X/752/2/111

Newman, S. F., Genzel, R., Förster-Schreiber, N. M., et al.
2012b, ApJ, 761, 43, doi: 10.1088/0004-637X/761/1/43

Newman, S. F., Buschkamp, P., Genzel, R., et al. 2014,
ApJ, 781, 21, doi: 10.1088/0004-637X/781/1/21

Oke, J. B., Cohen, J. G., Carr, M., et al. 1995, PASP, 107,
375, doi: 10.1086/133562

Oppenheimer, B. D., & Davé, R. 2008, MNRAS, 387, 577,
doi: 10.1111/j.1365-2966.2008.13280.x

Peeples, M. S., Werk, J. K., Tumlinson, J., et al. 2014, ApJ,
786, 54, doi: 10.1088/0004-637X/786/1/54

Prusinski, N. Z., Erb, D. K., & Martin, C. L. 2021, AJ, 161,
212, doi: 10.3847/1538-3881/abe85b

Reddy, N. A., Topping, M. W., Shapley, A. E., et al. 2022, ApJ, 926, 31, doi: 10.3847/1538-4357/ac3b4c

Roberts-Borsani, G. W., & Saintonge, A. 2019, MNRAS, 482, 4111, doi: 10.1093/mnras/sty2824

Roberts-Borsani, G. W., Saintonge, A., Masters, K. L., & Stark, D. V. 2020, MNRAS, 493, 3081, doi: 10.1093/mnras/staa464

Rodighiero, G., Daddi, E., Baronchelli, I., et al. 2011, ApJL, 739, L40, doi: 10.1088/2041-8205/739/2/L40

Rubin, K. H. R., Prochaska, J. X., Koo, D. C., et al. 2014, ApJ, 794, 156, doi: 10.1088/0004-637X/794/2/156

Rupke, D. S., Veilleux, S., & Sanders, D. B. 2005, ApJS, 160, 115, doi: 10.1086/432889

Sanders, R. L., Shapley, A. E., Kriek, M., et al. 2018, ApJ, 858, 99, doi: 10.3847/1538-4357/aabcbd

Sanders, R. L., Shapley, A. E., Jones, T., et al. 2021, ApJ, 914, 19, doi: 10.3847/1538-4357/abf4c1

Scannapieco, E., Silk, J., & Bouwens, R. 2005, ApJL, 635, L13, doi: 10.1086/499271

Shapiro, K. L., Genzel, R., Quataert, E., et al. 2009, ApJ, 701, 955, doi: 10.1088/0004-637X/701/2/955

Shapley, A. E., Steidel, C. C., Pettini, M., & Adelberger, K. L. 2003, ApJ, 588, 65, doi: 10.1086/373922

Sharma, M., & Nath, B. B. 2012, The Astrophysical Journal, 750, 55, doi: 10.1088/0004-637X/750/1/55

Somerville, R. S., Hopkins, P. F., Cox, T. J., Robertson, B. E., & Hernquist, L. 2008, MNRAS, 391, 481, doi: 10.1111/j.1365-2966.2008.13805.x

Speagle, J. S., Steinhardt, C. L., Capak, P. L., & Silverman, J. D. 2014, ApJS, 214, 15, doi: 10.1088/0067-0049/214/2/15

Steidel, C. C., Erb, D. K., Shapley, A. E., et al. 2010, ApJ, 717, 289, doi: 10.1088/0004-637X/717/1/289

Steidel, C. C., Shapley, A. E., Pettini, M., et al. 2004, ApJ, 604, 534, doi: 10.1086/381960

Sugahara, Y., Ouchi, M., Lin, L., et al. 2017, ApJ, 850, 51, doi: 10.3847/1538-4357/aa956d

Swinbank, A. M., Harrison, C. M., Tiley, A. L., et al. 2019, MNRAS, 487, 381, doi: 10.1093/mnras/stz1275

Tacconi, L. J., Genzel, R., Saintonge, A., et al. 2018, ApJ, 853, 179, doi: 10.3847/1538-4357/aaa4b4

Talia, M., Mignoli, M., Cimatti, A., et al. 2012, A&A, 539, A61, doi: 10.1051/0004-6361/201117683

Thompson, T. A., Quataert, E., & Murray, N. 2005, ApJ, 630, 167, doi: 10.1086/431923

Topping, M. W., Shapley, A. E., Reddy, N. A., et al. 2020, MNRAS, 495, 4430, doi: 10.1093/mnras/staa1410

Tremonti, C. A., Heckman, T. M., Kauffmann, G., et al. 2004, ApJ, 613, 898, doi: 10.1086/423264

Tumlinson, J., Peeples, M. S., & Werk, J. K. 2017, ARA&A, 55, 389, doi: 10.1146/annurev-astro-091916-055240

Übler, H., Naab, T., Oser, L., et al. 2014, MNRAS, 443, 2092, doi: 10.1093/mnras/stu1275

van der Wel, A., Bell, E. F., Häussler, B., et al. 2012, ApJS, 203, 24, doi: 10.1088/0067-0049/203/2/24

van Dokkum, P. G., Nelson, E. J., Franx, M., et al. 2015, ApJ, 813, 23, doi: 10.1088/0004-637X/813/1/23

Veilleux, S., Cecil, G., & Bland-Hawthorn, J. 2005, Annual Review of Astronomy and Astrophysics, 43, 769, doi: 10.1146/annurev.astro.43.072103.150610

Verhamme, A., Schaerer, D., & Maselli, A. 2006, A&A, 460, 397, doi: 10.1051/0004-6361:20065554

Vogelsberger, M., Genel, S., Sijacki, D., et al. 2013, MNRAS, 436, 3031, doi: 10.1093/mnras/stt1789

Weiner, B. J., Coil, A. L., Prochaska, J. X., et al. 2009, ApJ, 692, 187, doi: 10.1088/0004-637X/692/1/187

Weldon, A., Reddy, N. A., Topping, M. W., et al. 2022, MNRAS, 515, 841, doi: 10.1093/mnras/stac1822

—. 2023, MNRAS, 523, 5624, doi: 10.1093/mnras/stad1615

Whitaker, K. E., Franx, M., Leja, J., et al. 2014, ApJ, 795, 104, doi: 10.1088/0004-637X/795/2/104

Wisnioski, E., Förster Schreiber, N. M., Wuyts, S., et al. 2015, ApJ, 799, 209, doi: 10.1088/0004-637X/799/2/209

Wisnioski, E., Förster Schreiber, N. M., Fossati, M., et al. 2019, ApJ, 886, 124, doi: 10.3847/1538-4357/ab4db8

Wuyts, S., Förster Schreiber, N. M., Lutz, D., et al. 2011, ApJ, 738, 106, doi: 10.1088/0004-637X/738/1/106